Simulation of the Deformation for Cycling Chemo-Mechanically Coupled Battery Active Particles with Mechanical Constraints

R. Schoof[a,*], G. F. Castelli[b], W. Dörfler[a]

[a]*Karlsruhe Institute of Technology (KIT), Institute for Applied and Numerical Mathematics (IANM), Englerstr. 2, 76131 Karlsruhe, Germany*
[b]*Karlsruhe Institute of Technology (KIT), Institute of Thermal Process Engineering (TVT), Kaiserstr. 12, 76131 Karlsruhe, Germany*

Abstract

Next-generation lithium-ion batteries with silicon anodes have positive characteristics due to higher energy densities compared to state-of-the-art graphite anodes. However, the large volume expansion of silicon anodes can cause high mechanical stresses, especially if the battery active particle cannot expand freely. In this article, a thermodynamically consistent continuum model for coupling chemical and mechanical effects of electrode particles is extended by a change in the boundary condition for the displacement via a variational inequality. This switch represents a limited enlargement of the particle swelling or shrinking due to lithium intercalation or deintercalation in the host material, respectively. For inequality constraints as boundary condition a smaller time step size is need as well as a locally finer mesh. The combination of a primal-dual active set algorithm, interpreted as semismooth Newton method, and a spatial and temporal adaptive algorithm allows the efficient numerical investigation based on a finite element method. Using the example of silicon, the chemical and mechanical behavior of one- and two-dimensional representative geometries for a charge-discharge cycle is investigated. Furthermore, the efficiency of the adaptive algorithm is demonstrated. It turns out that the size of the gap has a significant influence on the maximal stress value and the slope of the increase. Especially in two space dimensions, the obstacle can cause an additional region with a lithium-poor phase.

Keywords: lithium-ion battery, finite deformation, obstacle problem, semismooth Newton method, finite elements, numerical simulation
2020 MSC: 74S05, 65M22, 90C33

1. Introduction

To meet the challenges of climate change, lithium-ion batteries have emerged as an important and desirable form of energy storage. The high energy density and long life time of the electrochemical storage system of lithium-ion batteries is crucial for mobile applications [1].

In addition, batteries with silicon anodes have proven to be very promising, since their nearly tenfold theoretical capacity compared to graphite ones currently in use [2–4]. However, the additional storage of lithium-ions can lead to a volume expansion up to 300% [5]. The large mechanical stresses occurring as a consequence during the lithiation and delithiation inside the host material can finally lead to particle fracture and therefore cause an undesired shorter battery lifetime and faster aging process [6, 7]. Improving the understanding of the degradation mechanism for lithium-ion batteries with new materials is an important step towards a sustainable future.

The coupling of chemical and mechanical effects inside the battery active particles is of great interest to understand the occurrence of the mechanical and diffusion-induced stress inside the host material [8]. For example for phase separating materials like lithium manganese oxide spinel $Li_xMn_2O_4$ (LMO), lithium iron phosphate Li_xFePO_4 (LFP) or sodium iron phosphate Na_xFePO_4 (NFP), the stresses are caused by a volume mismatch between lithium-poor and lithium-rich phases during the intercalation and deintercalation process [7–11].

For the coupling of phase separating materials with elastic properties, the Cahn–Hilliard theory [12, 13] can be extended with mechanical effects resulting in the Cahn–Larché approach [14–16] with small deformations and furthermore with finite deformations [11, 17–19]. These models have been used in recent years to simulatively investigate the intercalation of lithium for many different materials, e.g., see for $Li_xMn_2O_4$ [11, 20, 21], Li_xFePO_4 [17, 22–25], Na_xFePO_4 [24, 26, 27] or silicon [28–32] and the references therein.

All previous simulations of battery active particles have in common that the considered geometries can freely swell and are not limited in their volume enlargement. However, external conditions can change the boundary condition for the displacement, such as environmental pressure changes or the contact with the battery case, the current collector or other electrode particles. This limitation of volume is especially of great significance for the large volume change of silicon. In these situations contact problems occur, see for detailed information [33, 34]. There are different possibilities to capture such changes in boundary conditions with various advantages and disadvantages like *penalty formulation*, *augmented Lagrangian formulation* or *dual Lagrange multipliers*, compare [35, Section 17] and [36–41] and the references therein. The obstacle boundary condition can be written as *Karush–Kuhn–Tucker* (KKT) complementary conditions. The equations are also called *Signorini conditions*, because of their first formulation by Signorini [42, 43] for the unilateral normal contact.

The *primal-dual active set strategy* is an efficient technique for this kind of inequality constraints and can be interpreted as *semismooth Newton method*, compare [39, 44–49] and `deal.II` tutorial step-41 in [50]. An additional ansatz with a direct approach for Signorini's problem with small deformations and linear elasticity is investigated in [51]. In case of time-dependent problems coupled with inequality boundary constraints there are several numerical solution approaches [49, 52–55]. The dual Lagrange multiplier ansatz has the advantage that there is no need to change the system size. Furthermore, this method fulfills the obstacle boundary inequality constraints in the weak integral sense and the condition number of the system matrix does not change [37].

The numerical simulation of battery active particles with limited swelling due to inequality constrains at the boundary is computationally challenging because the contact region, which requires a higher grid resolution, changes in time. Space and time adaptivity is crucial to properly capture all relevant effects. Additionally, the switch from charging to discharging a lithium-ion battery for long term cycle investigations needs an appropriate mechanism for space and time control.

In [28, 29], a phase separation ansatz is used to model the intercalation of silicon. Following [56], however, a two-phase lithiation mechanism occurs only in the first half cycle of lithiation and therefore will not be considered in this paper. In particular, in [31] a measured open circuit voltage (OCV) curve is used for the chemical energy density in combination with a linear elastic approach to model the elastic deformation. A further possibility would be a Neo-Hookean ansatz as in [19] for the mechanical deformation.

In this article, we rely on the developed model approach by [31] for silicon with a finite deformation ansatz. We combine the large volume expansion with the inequality constraints for an obstacle boundary problem to simulate particle swelling in a limited space. The primal-dual active set strategy is derived, applied as semismooth Newton method and added to the spatial and temporal adaptive solution algorithm by [22, 23, 57] with higher finite element order and a fully variable order, variable time step size time integration scheme. This makes it possible to consider various parameter setups and one- and two-dimensional geometrical setups due to large computational savings introduced by the adaptive algorithm.

The remaining paper is structured as follows: in Section 2, we present our model to characterize the chemical-mechanical coupling with the obstacle boundary condition during one charging and discharging cycle. Next, we derive the semismooth Newton method from the primal-dual active set algorithm and combine it with a space and time adaptive algorithm. Section 4 discusses the simulation results for the developed model with obstacle contact. Finally, we summarize our main findings in Section 5.

2. Theory

In this section, we review and summarize the theory from [22, 31, 37] to formulate the coupled chemical and mechanical particle obstacle problem for battery active particles. For this we state a thermodynamically consistent theory for the chemo-mechanical coupling for (de-)lithiation with inequality boundary constraints to an obstacle problem. In a first step, we introduce the finite deformation theory for the particle and then couple the chemical and
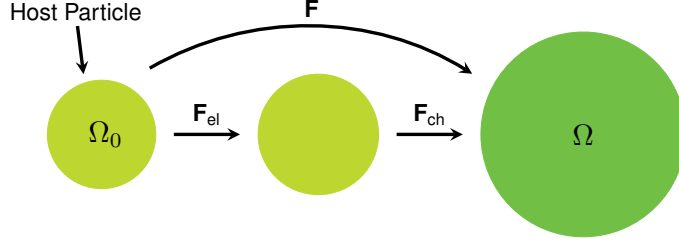
Figure 1: The total deformation $\mathbf{F}$ can be multiplicatively decomposed into an elastic part $\mathbf{F}_{\mathrm{el}}$ and a chemical part $\mathbf{F}_{\mathrm{ch}}$, compare [32, Figure 1].

mechanical effects with a common free energy density. After derivation of the equations for chemistry and mechanics, we incorporate the boundary constraints for the representation of an obstacle hindering the particle to expand freely. Since we consider the intercalation and deintercalation of lithium into and out of the host material, we simplify our wording and combine *lithiation and delithiation* as well as *charging and discharging* in the word *cycling*. A selection of abbreviations and symbols of our work is listed in Appendix A and some notation explanations notation are given in Appendix B.

2.1. Finite Deformation

To model the particle deformation during cycling, we consider a motion $\boldsymbol{x}(t, \boldsymbol{X}_0) = \chi(t, \boldsymbol{X}_0) = \boldsymbol{X}_0 + \boldsymbol{u}(t, \boldsymbol{X}_0)$ with a mapping $\chi \colon \mathbb{R}_{\geq 0} \times \Omega_0 \to \Omega$. Here, $\boldsymbol{X}_0 \in \Omega_0$ corresponds to an arbitrary point in the Lagrangian reference configuration Ω_0 which is mapped to a point $\boldsymbol{x} \in \Omega$ in the current Eulerian configuration Ω. The reversible total deformation gradient tensor $\mathbf{F}$ is defined as $\mathbf{F} = \partial \chi / \partial \boldsymbol{X}_0$ [58, Chapter 2.4]. This results in the relation $\mathbf{F} = \mathbf{Id} + \boldsymbol{\nabla}_0 \boldsymbol{u}$ with the identity matrix $\mathbf{Id}$ and the gradient of the displacement $\boldsymbol{\nabla}_0 \boldsymbol{u}$ with respect to the spatial coordinates of the reference configuration, compare [59, Chapter VI§1] and [58, Section 2.4]. We follow [31] and multiplicatively decompose the deformation gradient as $\mathbf{F} = \mathbf{F}_{\mathrm{ch}} \mathbf{F}_{\mathrm{el}}$. A sketch of this decomposition is given in Figure 1. The elastic part $\mathbf{F}_{\mathrm{el}}$ occurs due to mechanical stress, whereas the chemical part results from the changes in the lithium concentration. With an isotropic and linear chemical expansion of the active material the chemical part of the deformation gradient is given by $\mathbf{F}_{\mathrm{ch}} = \lambda_{\mathrm{ch}} \mathbf{Id}$ with $\lambda_{\mathrm{ch}} = \sqrt[3]{1 + v_{\mathrm{pmv}} c}$, where v_{pmv} defines the partial molar volume of the host material and c the lithium concentration [22].

2.2. Free Energy

Based on a free energy density ψ, we use a thermodynamically consistent model to guarantee a strictly positive entropy production [31, 60–62]. Following [31], we define the free energy density ψ as

$$\psi(c, \boldsymbol{\nabla}_0 \boldsymbol{u}) = \psi_{\mathrm{ch}}(c) + \psi_{\mathrm{el}}(c, \boldsymbol{\nabla}_0 \boldsymbol{u}), \tag{1}$$

combining chemical and mechanical effects. Adding an interfacial part $\psi_{\mathrm{int}}(\boldsymbol{\nabla} c)$ to Equation (1) for materials with phase separation leads to the classical Cahn–Hilliard approach combined with elasticity [17, 22, 26, 63, 64].

For the definition of the chemical part ψ_{ch} we use the experimentally obtained OCV curve U_{OCV} [31, 60, 65–67]

$$\psi_{\mathrm{ch}}(c) = - \int_0^{c/c_{\mathrm{max}}} F \, U_{\mathrm{OCV}}(z) \, \mathrm{d}z \tag{2}$$

with the Faraday constant F. For the elastic part ψ_{el} we use the linear elastic approach (Saint Venant–Kirchhoff model) as in [58, Section 6.5], [59, Chapter VI §3] and [22, 31]

$$\psi_{\mathrm{el}} = \frac{1}{2} \mathbf{E}_{\mathrm{el}} : \mathbb{C}\,[\mathbf{E}_{\mathrm{el}}] \qquad \text{with} \qquad \mathbb{C}\,[\mathbf{E}_{\mathrm{el}}] = \lambda_{\mathrm{H}} \mathrm{tr}(\mathbf{E}_{\mathrm{el}}) \mathbf{Id} + 2 G_{\mathrm{H}} \mathbf{E}_{\mathrm{el}}, \tag{3}$$

first and second Lamé constants $\lambda_{\mathrm{H}} = 2 G_{\mathrm{H}} \nu / (1 - 2\nu)$ and $G_{\mathrm{H}} = \mathrm{E}_{\mathrm{H}} / [2 (1 + 2\nu)]$, Young's modulus E_{H} and Poisson's ratio ν. Furthermore, we define the elastic strain tensor $\mathbf{E}_{\mathrm{el}}$, also called Green–Lagrange strain tensor, in our model by

$$\mathbf{E}_{\mathrm{el}} = \frac{1}{2} \left(\mathbf{F}_{\mathrm{el}}^{\mathsf{T}} \mathbf{F}_{\mathrm{el}} - \mathbf{Id} \right) = \frac{1}{2} \left(\lambda_{\mathrm{ch}}^{-2} \mathbf{F}^{\mathsf{T}} \mathbf{F} - \mathbf{Id} \right). \tag{4}$$

3

2.3. Elastic Deformation

A momentum balance law governs the mechanical behavior for the deformation in the Lagrangian frame

$$\mathbf{0} = -\boldsymbol{\nabla}_0 \cdot \mathbf{P} \qquad \text{in } (0, t_{\text{end}}) \times \Omega_0 \tag{5}$$

without considering any body or inertial forces [22, 31]. The first Piola–Kirchhoff stress tensor $\mathbf{P}$ and the Cauchy stress $\boldsymbol{\sigma}$ in the Eulerian frame are coupled via $\mathbf{P} = \det(\mathbf{F}) \boldsymbol{\sigma} \mathbf{F}^{-\top}$ [58, Section 3.1] using Nanson's formula for a vector element of infinitesimally small surface area [58, Section 2.4]. A thermodynamically consistent derivation specifies the first Piola–Kirchhoff stress tensor $\mathbf{P}(c, \boldsymbol{\nabla}_0 \boldsymbol{u}) = \partial_{\mathbf{F}} \psi = \lambda_{\text{ch}}^{-2} \mathbf{F} \mathbb{C} [\mathbf{E}_{\text{el}}]$, compare [58, Section 6.1].

2.4. Chemistry

A continuity equation is used to describe the change of the lithium concentration inside the host material via

$$\partial_t c = -\boldsymbol{\nabla}_0 \cdot \boldsymbol{N} \qquad \text{in } (0, t_{\text{end}}) \times \Omega_0 \tag{6}$$

with the lithium flux $\boldsymbol{N} := -m(c, \boldsymbol{\nabla}_0 \boldsymbol{u}) \boldsymbol{\nabla}_0 \mu = -D(\partial_c \mu)^{-1} \boldsymbol{\nabla}_0 \mu$ and the diffusion coefficient D for lithium atoms inside the active material. The definition for the lithium flux $\boldsymbol{N}$ follows [31] to guarantee positive entropy production. The chemical potential $\mu = \partial_c \psi$ is stated as the variational derivative of the Ginzburg–Landau free energy $\Psi = \int_{\Omega_0} \psi \, \mathrm{d}X_0$ [68]. This leads to the definition of the chemical potential

$$\mu = \partial_c \psi = -F U_{\text{OCV}} - \frac{v_{\text{pmv}}}{3} \lambda_{\text{ch}}^{-5} \left(\mathbf{F}^{\top} \mathbf{F} \right) : \mathbb{C} [\mathbf{E}_{\text{el}}] = -F U_{\text{OCV}} - \frac{v_{\text{pmv}}}{3 \lambda_{\text{ch}}^3} \mathbf{P} : \mathbf{F}. \tag{7}$$

The representative particle is cycled with a uniform and constant external flux N_{ext} with either positive or negative sign. This external flux is applied at the boundary of Ω_0 and measured in terms of the C-rate, for which we refer to [22]. With this definition, the simulation time t and the state of charge (SOC) can be related by

$$\text{SOC} = \frac{1}{V_{\Omega_0}} \int_{\Omega_0} \frac{c}{c_{\text{max}}} \, \mathrm{d}X_0 = \frac{c_0}{c_{\text{max}}} + N_{\text{ext}} \, [\text{C}] \cdot t[\text{h}] \tag{8}$$

with the volume V_{Ω_0} of Ω_0 and a constant initial condition $c_0 \in [0, c_{\text{max}}]$.

2.5. Obstacle Contact Problem

In the situation of a freely expanding particle during cycling, a stress-free boundary condition in normal direction is assumed on the particle surface [22, 32]:

$$\mathbf{P} \cdot \boldsymbol{n}_0 = \mathbf{0} \qquad \text{on } (0, t_{\text{end}}) \times \partial\Omega_0, \tag{9}$$

where $\boldsymbol{n}_0$ is the outer unit vector of the reference configuration Ω_0. However, if we consider a situation where the particle can no longer expand freely, this boundary condition must be adapted. This means that we have to handle a contact problem as restriction for the particle swelling.

A schematic sketch of a lithiation and delithiation cycle is shown in Figure 2: for example, the cross section of a lithium-poor particle is surrounded by a square shaped obstacle. The particle increases until it gets in contact with the obstacle. Now, the stress-free boundary condition in normal direction is replaced by a restriction of the displacement and thus, nonzero stresses in normal direction are possible. During delithiation, the particle detaches from the obstacle and shrinks again until it returns to a lithium-poor state. In the following, we replace the stress-free boundary condition in Equation (9) by an appropriate condition to incorporate the obstacle contact. As in [39, 47] we take the new boundary condition:

$$
\begin{cases}
\boldsymbol{u} \leq \boldsymbol{g} & \text{on } (0, t_{\text{end}}) \times \partial\Omega, \tag{10a} \\
\boldsymbol{\sigma} \cdot \boldsymbol{n} \leq \mathbf{0} & \text{on } (0, t_{\text{end}}) \times \partial\Omega, \tag{10b} \\
[\boldsymbol{\sigma} \cdot \boldsymbol{n}] [\boldsymbol{u} - \boldsymbol{g}] = \mathbf{0} & \text{on } (0, t_{\text{end}}) \times \partial\Omega, \tag{10c}
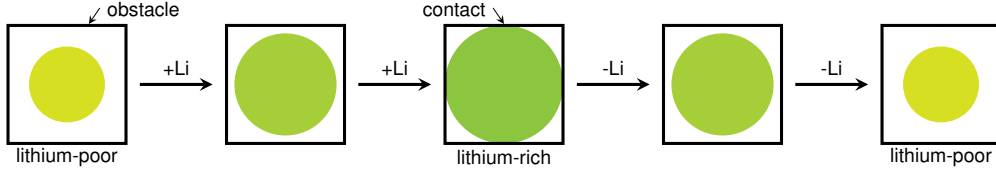\end{cases}
$$

4

Figure 2: Schematic sketch of lithiation and following delithiation of a representative battery active particle with volume change, getting in contact with the obstacle and detaching from the obstacle again.

understood componentwise as introduced in Appendix B, with outer unit vector $\boldsymbol{n}$ of the current configuration Ω.

Let $\hat{G}$ be the set that encloses Ω_0, i.e., $\Omega_0 \subset \hat{G}$, with boundary $\partial\hat{G}$ that defines the (time-independent) obstacle. We define $\hat{\boldsymbol{g}} \colon \partial\Omega_0 \to \partial\hat{G}$, $X_0 \mapsto \hat{\boldsymbol{g}}(X_0)$ as the projection of an arbitrary point X_0 on $\partial\Omega_0$ to the nearest boundary point on $\partial\hat{G}$ for each component parallel to the coordinate axes. Now, we set the *gap function* to $\boldsymbol{g} \colon \partial\Omega_0 \to \mathbb{R}^d_{>0}$, $\boldsymbol{g}(X_0) \coloneqq \hat{\boldsymbol{g}}(X_0) - X_0$, indicated in Figure 5. Equation (10a) thus means that the time dependent displacement $\boldsymbol{u}$ must componentwise be smaller or equal to the gap function $\boldsymbol{g}$ between the particle and the obstacle. Furthermore, Equation (10b) expresses the fact that for each component, the Cauchy stress tensor in normal direction is zero or less than zero. The latter case indicates compressive stress for the respective coordinate component. The last Equation (10c) is the complementary condition and specifies that one of the two Equations (10a) or (10b) must be zero, whereas the other condition can be nonzero. Again, this is interpreted componentwise for each component of the underlying coordinate system. For example, it is also possible for the complementary condition, that in the first component the displacement equals the gap function and there is compressive stress in the first component of the Cauchy stress vector in normal direction, but in the second component the Cauchy stress vector in normal direction is zero and the displacement component is smaller than the gap function component. In short: if the particle is not in contact with the obstacle, there must be zero stress in each component of the Cauchy stress tensor in normal direction, or vice versa, if there are compressive stresses, the particle has to be in contact with the obstacle in each component. This kind of boundary obstacle problem is also known as *Signorini problem* or thin obstacle problem [69, Section 1.11].

Since we formulate all constitutive equations in the Lagrangian domain, we use Nanson's formula and it follows for Equation (10):

$$\begin{cases} \boldsymbol{u} - \boldsymbol{g} \leq \boldsymbol{0} & \text{on } (0, t_{\text{end}}) \times \partial\Omega_0, & \text{(11a)} \\ -\mathbf{P} \cdot \boldsymbol{n}_0 \geq \boldsymbol{0} & \text{on } (0, t_{\text{end}}) \times \partial\Omega_0, & \text{(11b)} \\ [-\mathbf{P} \cdot \boldsymbol{n}_0][\boldsymbol{u} - \boldsymbol{g}] = \boldsymbol{0} & \text{on } (0, t_{\text{end}}) \times \partial\Omega_0. & \text{(11c)} \end{cases}$$

To solve this type of inequality boundary constraints, we employ a *primal-dual active set algorithm* [37, 44]. This algorithm is introduced in Section 3 and will be included in the numerical solution algorithm interpreted as *semismooth Newton algorithm* [39].

3. Numerical Approach

This sections deals with the numerical treatment of the model equations. Firstly, the normalization and mathematical problem is stated. Secondly, the steps for solving the initial boundary value problem are stated including a formulation for the space discretization with finite elements, time discretization and the primal-dual active set algorithm as semismooth Newton method. Finally, we incorporate the semismooth Newton method in the adaptive space and time integration scheme [22] and propose the numerical solution algorithm for the obstacle problem.

3.1. Problem Formulation

First, we improve the numerical stability by introducing a nondimensionalization of the model equations. The C-rate specifies the hours for the charging of the particle. We use the cycle time $t_{\text{cycle}} = 1/\text{C-rate}$ for the time scale, the particle radius L_0 in the Lagrangian frame for the spatial scale and the maximal concentration c_{max} as reference concentration. All dimensionless variables are collected in Table 1. The dimensionless number $\tilde{\text{E}}_{\text{H}}$ is used to relate the

$\tilde{t} = t/t_{\text{cycle}}$	$\tilde{X}_0 = X_0/L_0$	$\tilde{u} = u/L_0$	$\tilde{c} = c/c_{\text{max}}$	$\tilde{v} = vc_{\text{max}}$
$\tilde{U}_{\text{OCV}} = FU_{\text{OCV}}/R_{\text{gas}}T$	$\tilde{\mathrm{E}}_{\text{H}} = \mathrm{E}_{\text{H}}/R_{\text{gas}}Tc_{\text{max}}$	$\tilde{N}_{\text{ext}} = N_{\text{ext}}t_{\text{cycle}}/L_0c_{\text{max}}$	$\mathrm{Fo} = Dt_{\text{cycle}}/L_0^2$	

mechanical energy scale to the chemical energy scale, while the dimensionless *Fourier number* Fo is used to relate the diffusion time scale to the process time scale. From now, these dimensionless quantities are considered for the model equations, however, we neglect accentuation to improve readability.

For a general mathematical problem formulation, we follow the approach of [22] and solve our set of equations for the concentration c, the chemical potential μ and the displacement $\boldsymbol{u}$. The mixed formulation of the Cahn–Hilliard-type equations would allow to easily integrate the interfacial energy density for accounting phase separation. The deformation gradient $\mathbf{F}$, the strain tensor $\mathbf{E}_{\text{el}}$ as well as the stress tensors $\mathbf{P}$ and $\boldsymbol{\sigma}$ are calculated via the concentration c and the displacement $\boldsymbol{u}$.

The dimensionless initial boundary value problem with inequality boundary conditions is given as: let $t_{\text{end}} > 0$ be the final simulation time and $\Omega_0 \subset \mathbb{R}^d$ a representative bounded electrode particle as reference configuration with dimension $d = 3$. Find the normalized concentration $c\colon [0, t_{\text{end}}] \times \overline{\Omega}_0 \to [0, 1]$, the chemical potential $\mu\colon [0, t_{\text{end}}] \times \overline{\Omega}_0 \to \mathbb{R}$ and the displacement $\boldsymbol{u}\colon [0, t_{\text{end}}] \times \overline{\Omega}_0 \to \mathbb{R}^d$ satisfying

$$
\begin{cases}
\partial_t c = -\boldsymbol{\nabla}_0 \cdot N(c, \boldsymbol{\nabla}_0\mu, \boldsymbol{\nabla}_0\boldsymbol{u}) & \text{in } (0, t_{\text{end}}) \times \Omega_0, & \text{(12a)} \\
\mu = \partial_c \psi(c, \boldsymbol{\nabla}_0\boldsymbol{u}) & \text{in } (0, t_{\text{end}}) \times \Omega_0, & \text{(12b)} \\
\boldsymbol{0} = -\boldsymbol{\nabla}_0 \cdot \mathbf{P}(c, \boldsymbol{\nabla}_0\boldsymbol{u}) & \text{in } (0, t_{\text{end}}) \times \Omega_0, & \text{(12c)} \\
N \cdot \boldsymbol{n}_0 = N_{\text{ext}} & \text{on } (0, t_{\text{end}}) \times \partial\Omega_0, & \text{(12d)} \\
-\mathbf{P} \cdot \boldsymbol{n}_0 \geq \boldsymbol{0} & \text{on } (0, t_{\text{end}}) \times \partial\Omega_0, & \text{(12e)} \\
\boldsymbol{u} - \boldsymbol{g} \leq \boldsymbol{0} & \text{on } (0, t_{\text{end}}) \times \partial\Omega_0, & \text{(12f)} \\
[-\mathbf{P} \cdot \boldsymbol{n}_0]\,[\boldsymbol{u} - \boldsymbol{g}] = \boldsymbol{0} & \text{on } (0, t_{\text{end}}) \times \partial\Omega_0, & \text{(12g)} \\
c(0, \cdot) = c_0 & \text{in } \Omega_0 & \text{(12h)}
\end{cases}
$$

and an initial condition c_0 that is consistent with the boundary conditions. In case of lithiation we have a positive sign for the external lithium flux N_{ext} and in case of delithiation a negative sign. With appropriate boundary conditions for the displacement, rigid body motions are excluded. Note that the original formulation for the chemical deformation gradient $\mathbf{F}_{\text{ch}}$ is derived for the three-dimensional case, but all variables and equations are mathematically valid in lower dimensions as well.

3.2. Numerical Solution Procedure

In this subsection, we present all details for the numerical solution of our model equations: the space and time discretization of the initial boundary value problem (12), the interpretation of the primal-dual active set algorithm as semismooth Newton method and finally the proposed adaptive solution algorithm.

3.2.1. Weak Formulation

For the spatial discrete formulation, we derive the weak formulation of Equation (12). We define the function space $\boldsymbol{V}^* := H^1_*(\Omega_0; \mathbb{R}^d)$ which includes appropriate boundary constraints for the displacement considering possible boundary conditions without contact. These displacement boundary constraints are stated for the precise application case in Section 4. Furthermore, we declare the boundary on Ω_0 as $\Gamma_{\mathcal{P}} := \partial\Omega_0$ for the potential contact zone to be in contact with the obstacle. For the definitions of the scalar products, see Appendix B.

The weak solution can be derived from a minimization problem on a convex set, compare, e.g., [70, Chapter 1.2] or [51, 71, 72], or equivalently from a variational inequality, e.g. [69, Chapter 1.11], [73, Chapter 2.1], [74, Chapter II.6], [70, Chapter 1.2] or [51]. Multiplying with test functions, integration over the reference domain Ω_0 and

integration by parts, we state the weak formulation with a variational inequality in the third equation: find the solutions $c, \mu, \boldsymbol{u}$ with $c, \mu \in V := H^1(\Omega_0)$, $\partial_t c \in L^2(\Omega_0)$ and $\boldsymbol{u} \in V^+ := \{\boldsymbol{u} \in V^* : \boldsymbol{u} \le \boldsymbol{g}$ on $\Gamma_{\mathcal{P}}\}$ such that

$$
\begin{cases}
(\varphi, \partial_t c) = -\left(m(c, \boldsymbol{\nabla}_0 \boldsymbol{u}) \boldsymbol{\nabla}_0 \varphi, \boldsymbol{\nabla}_0 \mu\right) - (\varphi, N_{\text{ext}})_{\Gamma_{\mathcal{P}}}, & \text{(13a)} \\
0 = -(\varphi, \mu) + (\varphi, \partial_c \psi_{\text{ch}}(c) + \partial_c \psi_{\text{el}}(c, \boldsymbol{\nabla}_0 \boldsymbol{u})), & \text{(13b)} \\
0 \le (\boldsymbol{\nabla}_0 (\boldsymbol{\xi} - \boldsymbol{u}), \mathbf{P}(c, \boldsymbol{\nabla}_0 \boldsymbol{u})) & \text{(13c)}
\end{cases}
$$

for all test functions $\varphi \in V$ and $\boldsymbol{\xi} \in V^+$. For the formulation as saddle point problem, we follow [44, 46], deal.II tutorial step-41 in [50] and [48] and introduce the Lagrange multiplier $\boldsymbol{\lambda} := -\boldsymbol{\sigma} \cdot \boldsymbol{n} = -\mathbf{P} \cdot \boldsymbol{n}_0$.

3.2.2. Space Discretization

For the spatial discretization we choose a computational domain Ω_h that approximates the particle geometry Ω_0 by a polytop. To approximate the curved boundaries, we choose the isoparametric Lagrangian finite element method [59, Chapter III §2] on an admissible mesh $\mathcal{T}_n$. We define the finite dimensional Lagrangian finite element subspaces with the basis functions

$$
\begin{aligned}
V_h &= \text{span}\{\varphi_i : i = 1, \ldots, N\} \subset V, & \text{(14a)} \\
V_h^+ &= \text{span}\{\boldsymbol{\xi}_j : j = 1, \ldots, dN\} \subset V^+, & \text{(14b)} \\
\Lambda_h &= \text{span}\{\boldsymbol{\zeta}_k : k = 1, \ldots, dN_\Lambda\} \subset \Lambda, & \text{(14c)}
\end{aligned}
$$

where N denotes the number of degrees of freedom (DOFs) of the space V_h and N_Λ denotes the total number of nodes of the potential contact zone $\Gamma_{\mathcal{P}}$. For more details of the discretization, especially the discretization of the Lagrange multiplier space Λ_h, we refer to [37, 72, 75–77] and the references therein.

We now seek the discrete solutions for the concentration $c_h : [0, t_{\text{end}}] \to \{V_h : c_h \in [0, 1]\}$, the chemical potential $\mu_h : [0, t_{\text{end}}] \to V_h$, the displacement $\boldsymbol{u}_h : [0, t_{\text{end}}] \to V_h^*$ and the Lagrange multiplier $\lambda_h : [0, t_{\text{end}}] \to \Lambda_h$ of the spatial discrete saddle point problem of Equation (13).

In a next step, we want to add the finite element ansatz. Therefore, we represent the discrete solution variables with the basis functions given by

$$
c_h(t, \boldsymbol{X}_0) = \sum_{i=1}^{N} c_i(t) \varphi_i(\boldsymbol{X}_0), \qquad \mu_h(t, \boldsymbol{X}_0) = \sum_{i=1}^{N} \mu_i(t) \varphi_i(\boldsymbol{X}_0), \tag{15a}
$$

$$
\boldsymbol{u}_h(t, \boldsymbol{X}_0) = \sum_{j=1}^{dN} u_j(t) \boldsymbol{\xi}_j(\boldsymbol{X}_0), \qquad \lambda_h(t, \boldsymbol{X}_0) = \sum_{k=1}^{dN_\Lambda} \lambda_k(t) \boldsymbol{\zeta}_k(\boldsymbol{X}_0). \tag{15b}
$$

For the vector valued finite dimensional subspace $V_h^+ = \text{span}\{\boldsymbol{\xi}_j : j = 1, \ldots, dN\}$ and equivalent for Λ_h, we note ξ_j as the scalar basis function, which is the nonzero entry of the basis function vector $\boldsymbol{\xi}_j$ of node j. To simplify our notation, we use the same symbol for a function in V_h^+ and Λ_h as for its algebraic representation in terms of the nodal basis. For the concentration and the chemical potential, we use $\boldsymbol{c}_h$ and $\boldsymbol{\mu}_h$ for the algebraic representation.

Following [37, 44, 45] the biorthogonality of the basis functions has following property:

$$
\int_{\Gamma_{\mathcal{P}}} \boldsymbol{\xi}_j \cdot \boldsymbol{\zeta}_k \, \mathrm{d}\boldsymbol{S}_0 = \delta_{j,k} \int_{\Gamma_{\mathcal{P}}} \xi_j \, \mathrm{d}\boldsymbol{S}_0 \tag{16}
$$

for all $j = 1, \ldots, dN$ and $k = 1, \ldots, dN_\Lambda$. For Equation (16) we suppose that the basis function $\boldsymbol{\xi}_j$ and the basis function $\boldsymbol{\zeta}_j$ with the same index j are associated to the same node on $\Gamma_{\mathcal{P}}$. The Kronecker symbol $\delta_{j,k}$ can be interpreted as follows [37]:

$$
\delta_{j,k} = \begin{cases} 1, & \text{node } j \text{ coincides with potential contact node } k, \\ 0, & \text{otherwise.} \end{cases} \tag{17}
$$

At the end of the spatial discretization process, we want to formulate our problem as a discrete nonlinear differential algebraic equation (DAE) before we perform the time discretization in the next Subsection 3.2.3. We therefore have a closer look on the algebraic representation of our discrete weak formulation, in particular of the momentum balance equation and of the displacement inequality at the boundary condition (12f).

Let u_h and λ_h be the solution of the discrete variational inequality. Then, we have the algebraic representation of the discrete weak formulation of Equation (12c) as

$$\mathbf{P}_h(c_h, \nabla_0 u_h) + \mathbf{B}_h \lambda_h = \mathbf{0} \tag{18}$$

with the nonlinear vector

$$\mathbf{P}_h(c_h, \nabla_0 u_h) = \left[\int_{\Omega_0} \nabla_0 \xi_j : \mathbf{P}(c_h, \nabla_0 u_h) \, dX_0 \right]_{j=1,\ldots,dN} \tag{19}$$

and the matrix

$$\mathbf{B}_h = \left[\int_{\Gamma_\mathcal{P}} \xi_j \cdot \zeta_k \, dS_0 \right]_{j=1,\ldots,dN, \ k=1,\ldots,dN_\Lambda}. \tag{20}$$

With an appropriate node numbering, $\mathbf{B}_h$ can be written as $\mathbf{B}_h = (\mathbf{0}, \mathbf{D}_h)^\mathsf{T}$. Due to the biorthogonality in Equation (16), the diagonal matrix $\mathbf{D}_h$ has the entries

$$(D_h)_{j,k} = \int_{\Gamma_\mathcal{P}} \xi_j \cdot \zeta_k \, dS_0 = \delta_{j,k} \int_{\Gamma_\mathcal{P}} \xi_k \, dS_0 \tag{21}$$

for all $j, k = 1, \ldots, dN_\Lambda$. Now, we define two sets of indices: all degrees of freedom on $\Gamma_\mathcal{P}$ with $\mathcal{P}$ (all potential contact nodes) and all other nodes with $\mathcal{N}$.

Consider now the weaker integral condition for the strong pointwise non-penetration condition of Equation (12) for the discrete contact conditions for all $p \in \mathcal{P}$:

$$\int_{\Gamma_\mathcal{P}} u_h \cdot \zeta_p \, dS_0 \leq \int_{\Gamma_\mathcal{P}} g_h \cdot \zeta_p \, dS_0 =: \hat{g}_p \quad \Longleftrightarrow \quad \int_{\Gamma_\mathcal{P}} u_p \xi_p \zeta_p \, dS_0 \leq \hat{g}_p, \tag{22}$$

where u_p is the scalar coefficient of the discrete vector u_h of DOF p and g_h is an appropriate approximation of g on $\Gamma_\mathcal{P}$. Next, we rewrite Equation (22) with the help of Equation (21) for the algebraic representation of the weak non-penetration condition $\hat{u}_p := (D_h)_{p,p} u_p \leq \hat{g}_p$ for all $p \in \mathcal{P}$. Then, we can rewrite the condition for the Lagrange multiplier in the same way to get $\hat{\lambda}_p := (D_h)_{p,p} \lambda_p$ with the same definition for λ_p as for u_p for all nodes $p \in \mathcal{P}$.

Finally, the discrete algebraic form of the contact problem of Equation (12) is given by:

$$\mathbf{P}_h(c_h, \nabla_0 u_h) + \mathbf{B}_h \lambda_h = \mathbf{0}, \tag{23a}$$

$$\hat{u}_p \leq \hat{g}_p, \qquad \hat{\lambda}_p \geq 0, \qquad \hat{\lambda}_p(\hat{u}_p - \hat{g}_p) = 0 \tag{23b}$$

for all nodes $p \in \mathcal{P}$. Equation (23b) can also be identified as discrete KKT conditions of a constrained optimization problem for inequality constraints [44].

Next, we use a reformulation of the three equations of Equation (23b) based on the nonlinear complementarity problem (NCP) function

$$C(a, b) := b - \max(b + \alpha a, 0), \qquad \forall a, b \in \mathbb{R}, \tag{24}$$

and $\alpha > 0$ arbitrarily fixed [47]. The following equivalence is true [39, 47]:

$$C(a, b) = 0 \quad \Longleftrightarrow \quad a \leq 0, \ b \geq 0, \ ab = 0. \tag{25}$$

Applied to Equation (23b) it follows:

$$C(\hat{u}_p, \hat{\lambda}_p) = \hat{\lambda}_p - \max(\hat{\lambda}_p + \alpha(\hat{u}_p - \hat{g}_p), 0) = 0 \tag{26}$$
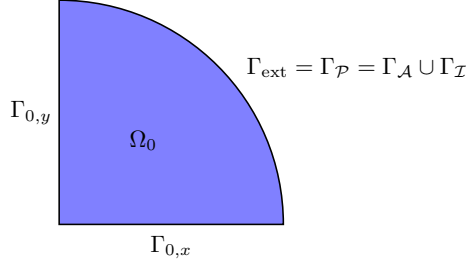
Figure 3: All boundary parts for the example of a two-dimensional quarter disk domain Ω_0 split up into two artificial boundaries $\Gamma_{0,y}$ and $\Gamma_{0,x}$ with additional Dirichlet constraints for the displacement $\boldsymbol{u}$ and the potential contact boundary $\Gamma_{\mathcal{P}}$ subdivided into the active contact boundary $\Gamma_{\mathcal{A}}$ and the inactive boundary $\Gamma_{\mathcal{I}}$.

for all $p \in \mathcal{P}$ and $\alpha > 0$. In total we rewrite Equation (23) to

$$\mathbf{P}_h(c_h, \boldsymbol{\nabla}_0 \boldsymbol{u}_h) + \mathbf{B}_h \boldsymbol{\lambda}_h = \mathbf{0}, \tag{27a}$$
$$\mathbf{C}_{\mathcal{P}}(\boldsymbol{u}_h, \boldsymbol{\lambda}_h) \qquad\quad = \mathbf{0} \tag{27b}$$

with the same definition for $\mathbf{C}_{\mathcal{P}}(\cdot, \cdot)$ in each component as in Equation (26) for all $p \in \mathcal{P}$, compare also Appendix B.

Considering for example an quarter shaped obstacle like in Figure 3, the physical boundary of Ω_0 can be defined as Γ_{ext}. $\Gamma_{0,y}$ and $\Gamma_{0,x}$ are two artificial boundaries with appropriate Dirichlet boundary conditions for the displacement $\boldsymbol{u}$. Γ_{ext} is the potential contact boundary $\Gamma_{\mathcal{P}}$ and splits into two parts, the active contact boundary $\Gamma_{\mathcal{A}}$ and the inactive boundary $\Gamma_{\mathcal{I}}$.

Collecting all time-dependent solution variables in a vector-valued function

$$\boldsymbol{y} \colon [0, t_{\text{end}}] \to \mathbb{R}^{(2+d)N+dN_\Lambda}, \quad t \mapsto \boldsymbol{y}(t) = \begin{pmatrix} \boldsymbol{c}_h \\ \boldsymbol{\mu}_h \\ \boldsymbol{u}_h \\ \boldsymbol{\lambda}_h \end{pmatrix} \tag{28}$$

we can state our spatial discrete problem of the saddle point formulation of Equation (13) as general nonlinear DAE: Find $\boldsymbol{y} \colon [0, t_{\text{end}}] \to \mathbb{R}^{(2+d)N+dN_\Lambda}$ satisfying

$$\mathbf{M} \partial_t \boldsymbol{y} = \boldsymbol{f}(t, \boldsymbol{y}) \qquad \text{for } t \in (0, t_{\text{end}}], \qquad \boldsymbol{y}(0) = \boldsymbol{y}^0. \tag{29}$$

On the left side, the system mass matrix $\mathbf{M}$ has only one nonzero-block entry $\mathbf{M}_h = \left[(\varphi_i, \varphi_j) \right]_{ij}$ and is therefore singular. $\mathbf{M}_h$ identifies the mass matrix of the finite element space V_h. On the right side, $\boldsymbol{f} \colon [0, t_{\text{end}}] \times \mathbb{R}^{(2+d)N+dN_\Lambda} \to \mathbb{R}^{(2+d)N+dN_\Lambda}$ is given according to the algebraic formulation in Equation (27) by

$$\boldsymbol{f}(t, \boldsymbol{y}) := \begin{pmatrix} -\mathbf{K}_m(c_h, \boldsymbol{\nabla}_0 \boldsymbol{u}_h) \boldsymbol{\mu}_h - N_{\text{ext}} \\ -\mathbf{M}_h \boldsymbol{\mu}_h + \boldsymbol{\Psi}_{\text{ch}}(c_h) + \boldsymbol{\Psi}_{\text{el}}(c_h, \boldsymbol{\nabla}_0 \boldsymbol{u}_h) \\ \mathbf{P}_h(c_h, \boldsymbol{\nabla}_0 \boldsymbol{u}_h) + \mathbf{B}_h \boldsymbol{\lambda}_h \\ \mathbf{C}_{\mathcal{P}}(\boldsymbol{u}_h, \boldsymbol{\lambda}_h) \end{pmatrix} \tag{30}$$

with the relation of $\boldsymbol{y}$ to the solution variables as in Equation (28). The quantities in the definition of $\boldsymbol{f}$ are given by the mass matrix $\mathbf{M}_h$, the stiffness matrix $\mathbf{K}_m(c_h, \boldsymbol{\nabla}_0 \boldsymbol{u}_h) = \left[\left(m(c_h, \boldsymbol{\nabla}_0 \boldsymbol{u}_h) \boldsymbol{\nabla}_0 \varphi_i, \boldsymbol{\nabla}_0 \varphi_j \right) \right]_{i,j}$, the vectors for the non-linearities $\boldsymbol{\Psi}_{\text{ch}}(c_h) = \left[(\varphi_i, \partial_c \psi_{\text{ch}}(c_h)) \right]_i$ and $\boldsymbol{\Psi}_{\text{el}}(c_h, \boldsymbol{\nabla}_0 \boldsymbol{u}_h) = \left[(\varphi_i, \partial_c \psi_{\text{el}}(c_h, \boldsymbol{\nabla}_0 \boldsymbol{u}_h)) \right]_i$, as well as the boundary condition $N_{\text{ext}} = \left[(\varphi_i, N_{\text{ext}})_{\Gamma_{\text{ext}}} \right]_i$. For the block mass matrix $\mathbf{B}_h$, the nonlinear vector $\mathbf{P}_h(c_h, \boldsymbol{\nabla}_0 \boldsymbol{u}_h)$ and the vector $\mathbf{C}_{\mathcal{P}}(\boldsymbol{u}_h, \boldsymbol{\lambda}_h)$, we refer to the definitions in Equations (19), (20) and (27b), respectively.

3.2.3. Time Discretization

For the temporal discretization, we follow the approach in [22] by using a variable-step, variable-order algorithm [78–81]. This approach seems reasonable since the DAE (29) can be treated in a similar way to a stiff ordinary differential equation. The algorithm adaptively changes the time step size $\tau_n > 0$ and the order by an error control.

This leads to the space and time discrete problem: find the discrete solution $y^{n+1} \approx y(t_{n+1})$ satisfying

$$\alpha_{k_n} \mathbf{M} \left(y^{n+1} - \boldsymbol{\Phi}^n \right) = \tau_n \boldsymbol{f} \left(t_{n+1}, y^{n+1} \right) \tag{31}$$

to advance one time step from t_n to $t_{n+1} = t_n + \tau_n$. $\boldsymbol{\Phi}^n$ is defined by the solutions on the former time steps $y^n, \ldots, y^{n-k}$ and a constant $\alpha_{k_n} > 0$ depending on the selected order k_n at time t_n [79, Section 2.3]. Because of the time-dependent Neumann boundary condition N_{ext}, the vector $\boldsymbol{f}$ does also explicitly depend on the time t.

3.2.4. The Primal-Dual Active Set Algorithm as Semismooth Newton Method

The next step is to use an appropriate iterative solution scheme to handle the NCP function in Equation (27b). The primal-dual active set algorithm is the strategy of choice, since it is an iterative approach to deal with the condition in Equation (27b) and to predict the next active and inactive set $\mathcal{A}_{k+1}^{n+1}$ and $\mathcal{I}_{k+1}^{n+1}$ for each new time step t_{n+1} [37, 39, 44].

For the moment, we consider only Equation (27a) and Equation (27b), which are the relevant parts for the contact inequality condition. To compute the new active and inactive set $\mathcal{A}_{k+1}^{n+1}$ and $\mathcal{I}_{k+1}^{n+1}$ on the potential boundary $\Gamma_{\mathcal{P}}$ in a new time step t_{n+1} we will use the *primal-dual active set algorithm*, compare [37, 39, 44].

Since we have to linearize Equation (31) anyway to handle the nonlinear algebraic system via the Newton–Raphson method, we can also use the interpretation of the primal-dual active set algorithm as semismooth Newton method, compare [39, 47, 48] and `deal.II` tutorials step-41 and step-42 in [50]. The locally superlinear convergence and global convergence results are shown in [39]. Since $C(\cdot, \cdot)$ in Equation (27b) is not differentiable, Newton techniques for solving Equation (27) have to be applicable with generalizations of the derivative of a function. These methods are named *generalized Newton methods*, see e.g. [47] and the references therein. In this paper we propose the *semismooth Newton method* following [39, 47]. The semismoothness characteristics of the max-operator in Equation (27b) lead to local convergence properties of the semismooth Newton method.

So we need a linearization of a function $C(\cdot, \cdot)$, being not classically differentiable. As a replacement, we can use the concept of slant differentiability, compare [47]. $C(\cdot, \cdot)$ is slantly differentiable with

$$\frac{\partial}{\partial u_p} C(\hat{u}_p, \hat{\lambda}_p) = \begin{cases} -\alpha \, (D_h)_{p,p}, & \text{if } \hat{\lambda}_p + \alpha(\hat{u}_p - \hat{g}_p) > 0, \\ 0, & \text{if } \hat{\lambda}_p + \alpha(\hat{u}_p - \hat{g}_p) \leq 0, \end{cases} \tag{32a}$$

$$\frac{\partial}{\partial \lambda_p} C(\hat{u}_p, \hat{\lambda}_p) = \begin{cases} 0, & \text{if } \hat{\lambda}_p + \alpha(\hat{u}_p - \hat{g}_p) > 0, \\ 1, & \text{if } \hat{\lambda}_p + \alpha(\hat{u}_p - \hat{g}_p) \leq 0. \end{cases} \tag{32b}$$

Recall the definition of the potential contact nodes $\mathcal{P} = \mathcal{A} \cup \mathcal{I}$, the active and inactive sets, respectively, and the remaining nodes $\mathcal{N}$. The set of all nodes is defined via $\mathcal{S} = \mathcal{P} \cup \mathcal{N}$. Moreover, we define for the Jacobian matrix the derivatives for the nonlinear part:

$$_z\mathbf{A}_h = \left[\left(\boldsymbol{\nabla}_0 \boldsymbol{\xi}_k, \partial_z \mathbf{P}(c_h^k, \boldsymbol{\nabla}_0 \boldsymbol{u}_h^k) \varphi_i \right) \right]_{k,i}, \qquad _{\mathbf{G}}\mathbf{A}_h = \left[\left(\boldsymbol{\nabla}_0 \boldsymbol{\xi}_k, \partial_{\mathbf{G}} \mathbf{P}(c_h^k, \boldsymbol{\nabla}_0 \boldsymbol{\xi}_l) \right) \right]_{k,l}, \tag{33}$$

for $i = 1, \ldots, N$ and $k, l = 1, \ldots, dN$, with the derivative regarding the first scalar valued quantity and the second tensor valued quantity, respectively. With the partitions of the matrices $_z\mathbf{A}_h$, $_{\mathbf{G}}\mathbf{A}_h$ and $\mathbf{B}_h$ as well as the vectors $\boldsymbol{u}_h$ and λ_h for the different sets, a semismooth Newton step for Equation (27) has the form

$$\begin{pmatrix} _z\mathbf{A}_{\mathcal{N}\mathcal{S}} & _{\mathbf{G}}\mathbf{A}_{\mathcal{N}\mathcal{N}} & _{\mathbf{G}}\mathbf{A}_{\mathcal{N}\mathcal{I}_k} & _{\mathbf{G}}\mathbf{A}_{\mathcal{N}\mathcal{A}_k} & \mathbf{0} & \mathbf{0} \\ _z\mathbf{A}_{\mathcal{I}_k\mathcal{S}} & _{\mathbf{G}}\mathbf{A}_{\mathcal{I}_k\mathcal{N}} & _{\mathbf{G}}\mathbf{A}_{\mathcal{I}_k\mathcal{I}_k} & _{\mathbf{G}}\mathbf{A}_{\mathcal{I}_k\mathcal{A}_k} & \mathbf{D}_{\mathcal{I}_k} & \mathbf{0} \\ _z\mathbf{A}_{\mathcal{A}_k\mathcal{S}} & _{\mathbf{G}}\mathbf{A}_{\mathcal{A}_k\mathcal{N}} & _{\mathbf{G}}\mathbf{A}_{\mathcal{A}_k\mathcal{I}_k} & _{\mathbf{G}}\mathbf{A}_{\mathcal{A}_k\mathcal{A}_k} & \mathbf{0} & \mathbf{D}_{\mathcal{A}_k} \\ \mathbf{0} & \mathbf{0} & \mathbf{0} & \mathbf{0} & \mathbf{Id}_{\mathcal{I}_k} & \mathbf{0} \\ \mathbf{0} & \mathbf{0} & \mathbf{0} & -\alpha \mathbf{D}_{\mathcal{A}_k} & \mathbf{0} & \mathbf{0} \end{pmatrix} \begin{pmatrix} \delta \boldsymbol{c}_{\mathcal{S}} \\ \delta \boldsymbol{u}_{\mathcal{N}} \\ \delta \boldsymbol{u}_{\mathcal{I}_k} \\ \delta \boldsymbol{u}_{\mathcal{A}_k} \\ \delta \lambda_{\mathcal{I}_k} \\ \delta \lambda_{\mathcal{A}_k} \end{pmatrix} = - \begin{pmatrix} \mathbf{P}_{\mathcal{N}}(c_h^k, \boldsymbol{\nabla}_0 \boldsymbol{u}_h^k) \\ \mathbf{P}_{\mathcal{I}_k}(c_h^k, \boldsymbol{\nabla}_0 \boldsymbol{u}_h^k) + \left(\mathbf{B}_h \lambda_h^k \right)_{\mathcal{I}_k} \\ \mathbf{P}_{\mathcal{A}_k}(c_h^k, \boldsymbol{\nabla}_0 \boldsymbol{u}_h^k) + \left(\mathbf{B}_h \lambda_h^k \right)_{\mathcal{A}_k} \\ \lambda_{\mathcal{I}_k}^k \\ -\alpha \left(\mathbf{D}_{\mathcal{A}_k} \boldsymbol{u}_{\mathcal{A}_k}^k - \boldsymbol{g}_{\mathcal{A}_k} \right) \end{pmatrix} \tag{34}$$

with the definition of Equation (22) for all active points $p \in \mathcal{A}_k$, for $\boldsymbol{g}_{\mathcal{A}_k}$ and $(\mathbf{B}_h)_{\mathcal{N}} = \mathbf{0}$. $\mathbf{Id}_{\mathcal{I}_k}$ is the identity matrix of dimension card $(\mathcal{I}_k)$.

As a next step we have a closer look at different subsystems of Equation (34). The fourth row provides

$$\lambda_{\mathcal{I}_k}^{k+1} = \lambda_{\mathcal{I}_k}^k + \delta \lambda_{\mathcal{I}_k} = \lambda_{\mathcal{I}_k}^k - \lambda_{\mathcal{I}_k}^k = \mathbf{0} \tag{35}$$

10

and the last one implies

$$\boldsymbol{u}_{\mathcal{A}_k}^{k+1} = \boldsymbol{u}_{\mathcal{A}_k}^k + \delta \boldsymbol{u}_{\mathcal{A}_k} = \boldsymbol{u}_{\mathcal{A}_k}^k + \mathbf{D}_{\mathcal{A}_k}^{-1} \boldsymbol{g}_{\mathcal{A}_k} - \boldsymbol{u}_{\mathcal{A}_k}^k = \mathbf{D}_{\mathcal{A}_k}^{-1} \boldsymbol{g}_{\mathcal{A}_k}. \tag{36}$$

Equation (35) and Equation (36) are exactly the conditions of the active and inactive sets in the primal-dual active set algorithm. Considering now the subsystem of Equation (34) for the active set of the Lagrange multiplier, we have

$$\boldsymbol{\lambda}_{\mathcal{A}_k}^{k+1} = \boldsymbol{\lambda}_{\mathcal{A}_k}^k + \delta \boldsymbol{\lambda}_{\mathcal{A}_k} = -\mathbf{D}_{\mathcal{A}_k}^{-1} \mathbf{P}_{\mathcal{A}_k}(c_h^k, \boldsymbol{\nabla}_0 \boldsymbol{u}_h^k) - \mathbf{D}_{\mathcal{A}_k}^{-1} ({}_\mathrm{G}\mathbf{A}_h \delta \boldsymbol{u})_{\mathcal{A}_k} - \mathbf{D}_{\mathcal{A}_k}^{-1} ({}_z\mathbf{A}_h \delta c)_{\mathcal{A}_k}. \tag{37}$$

This means that the Lagrange multiplier only has to be computed on the active set with the solutions δc and $\delta \boldsymbol{u}$.

Let us now consider for a moment the two sets $\mathcal{N}$ and $\mathcal{I}$ together as $\hat{\mathcal{S}}$ since the subsystems of Equation (34) for both sets are equal. The combination of the two sets results in

$$\begin{pmatrix} {}_z\mathbf{A}_{\hat{\mathcal{S}},\mathcal{S}} & {}_\mathrm{G}\mathbf{A}_{\hat{\mathcal{S}}} \end{pmatrix} \begin{pmatrix} \delta \boldsymbol{c}_{\mathcal{S}} \\ \delta \boldsymbol{u}_{\hat{\mathcal{S}}} \end{pmatrix} = - \begin{pmatrix} \mathbf{P}_{\hat{\mathcal{S}}}(c_h^k, \boldsymbol{\nabla}_0 \boldsymbol{u}_h^k) + {}_\mathrm{G}\mathbf{A}_{\hat{\mathcal{S}},\mathcal{A}_k} \delta \boldsymbol{u}_{\mathcal{A}_k} \end{pmatrix} \tag{38}$$

to compute $\boldsymbol{u}_{\hat{\mathcal{S}}}^{k+1}$. In the end we solve the reduced system for the Newton update

$$\begin{pmatrix} {}_z\mathbf{A}_{\mathcal{N}\mathcal{S}} & {}_\mathrm{G}\mathbf{A}_{\mathcal{N}\mathcal{N}} & {}_\mathrm{G}\mathbf{A}_{\mathcal{N}\mathcal{I}_k} & {}_\mathrm{G}\mathbf{A}_{\mathcal{N}\mathcal{A}_k} \\ {}_z\mathbf{A}_{\mathcal{I}_k\mathcal{S}} & {}_\mathrm{G}\mathbf{A}_{\mathcal{I}_k\mathcal{N}} & {}_\mathrm{G}\mathbf{A}_{\mathcal{I}_k\mathcal{I}_k} & {}_\mathrm{G}\mathbf{A}_{\mathcal{I}_k\mathcal{A}_k} \\ {}_z\mathbf{A}_{\mathcal{A}_k\mathcal{S}} & {}_\mathrm{G}\mathbf{A}_{\mathcal{A}_k\mathcal{N}} & {}_\mathrm{G}\mathbf{A}_{\mathcal{A}_k\mathcal{I}_k} & {}_\mathrm{G}\mathbf{A}_{\mathcal{A}_k\mathcal{A}_k} \end{pmatrix} \begin{pmatrix} \delta \boldsymbol{c}_{\mathcal{S}} \\ \delta \boldsymbol{u}_{\mathcal{N}} \\ \delta \boldsymbol{u}_{\mathcal{I}_k} \\ \delta \boldsymbol{u}_{\mathcal{A}_k} \end{pmatrix} = - \begin{pmatrix} \mathbf{P}_{\mathcal{N}}(c_h^k, \boldsymbol{\nabla}_0 \boldsymbol{u}_h^k) \\ \mathbf{P}_{\mathcal{I}_k}(c_h^k, \boldsymbol{\nabla}_0 \boldsymbol{u}_h^k) \\ \mathbf{P}_{\mathcal{A}_k}(c_h^k, \boldsymbol{\nabla}_0 \boldsymbol{u}_h^k) \end{pmatrix}, \tag{39}$$

restricting the Newton update to zero for the degrees of freedom in the active set and providing the correct boundary values to the new solution as inhomogeneous Dirichlet boundary values. This can be done via $\boldsymbol{u}_h^k := P_{\mathcal{A}_{k+1}}(\boldsymbol{u}_h^k)$ with the projection

$$P_{\mathcal{A}_{k+1}}(\boldsymbol{u}_h)_p := \begin{cases} \hat{u}_p, & \text{if } p \notin \mathcal{A}_{k+1}, \\ \hat{g}_p, & \text{if } p \in \mathcal{A}_{k+1}. \end{cases} \tag{40}$$

After solving the total Newton system and computing the new solutions, the Lagrange multiplier $\boldsymbol{\lambda}^{k+1}$ can be recovered via Equation (37) and Equation (35).

Following [37] we use

$$\boldsymbol{\lambda}_{\mathcal{A}_k}^{k+1} = \boldsymbol{\lambda}_{\mathcal{A}_k}^k + \delta \boldsymbol{\lambda}_{\mathcal{A}_k} = -\mathbf{D}_{\mathcal{A}_k}^{-1} \mathbf{P}_{\mathcal{A}_k}(c_h^{k+1}, \boldsymbol{\nabla}_0 \boldsymbol{u}_h^{k+1}) \tag{41}$$

which has the same linearization as Equation (37). This corresponds to an inexact strategy, compare Algorithm 3 in [37]. Further, it reduces the computational effort of a second nested loop compared to Algorithm 2 in [37]. However, the inexact case is an additional simplification of the applied algorithm used in this paper. This further means that it has not been clarified whether the superlinear convergence is retained [37].

Finally, we have to formulate a semismooth Newton algorithm in one time step. With the concept of the semismooth Newton algorithm we can also update our DAE (29) and we can remove all parts related with the Lagrange multiplier $\boldsymbol{\lambda}$. This results in a new definition of $\tilde{\boldsymbol{y}}, \tilde{\boldsymbol{f}} \in \mathbb{R}^{(2+d)N}$. In the following, we consider only the updated system and omit again the accentuation $\tilde{\Box}$. So we have to linearize the updated version of the DAE (31) to compute the Newton update.

3.2.5. Adaptive Solution Algorithm

After the linearization of the updated version of the DAE (31) with the semismooth Newton method, the Newton update is computed with a direct LU-decomposition. Keep in mind that the number of iteration steps during the Newton method can be reduced with an appropriate initialization. The starting values for the first time step are given in Subsection 4.1 whereas during time integration a predictor scheme is applied [79].

For the space and time adaptive solution algorithm we follow Algorithm 1 in [22]. Here, a temporal error estimator [78–81] and a spacial error estimator are applied. A gradient recovery estimator is used for the spatial regularity [82, Chapter 4]. To mark the cells for local coarsening and refinement, the parameters θ_c and θ_r are used with a

maximal strategy [83]. Finally, a mixed error control is applied using the parameters RelTol$_t$, AbsTol$_t$, RelTol$_x$ and AbsTol$_x$. Further details can be found in [22].

Combining the semismooth Newton method and the space and time adaptive algorithm by [22, Algorithm 1], we propose the following concept:

Algorithm 2 Semismooth Newton Method for Adaptive Obstacle Space Time Algorithm

---

1:   Initialize $\mathcal{A}_1^0$ and $\mathcal{I}_1^0$ such that $\mathcal{P}^0 = \mathcal{A}_1^0 \cup \mathcal{I}_1^0$ and $\mathcal{A}_1^0 \cap \mathcal{I}_1^0 = \emptyset$
2: **while** $t_n < t_{\text{end}}$ **do**
3:      Given $\mathcal{T}_n, \tau_n, k_n$ and $y^n, \ldots, y^{n-k_n}$, set $k = 1$
4:      Extrapolate $y^n, \ldots, y^{n-k_n}$ to compute predictor $y^{(0),n+1}$ in t_{n+1}
5:      **while** not converged **do**
6:          Solve for Newton update $\delta y^{k,n}$ (introducing the contact condition as additional Dirichlet
            boundary condition and set the Newton update to zero for DOFs in the active set)
7:          Compute $y^{k+1,n+1} = y^{k,n} + \delta y^{k,n}$
8:          Recover $\lambda^{k+1,n+1}$ and compute new $\mathcal{A}_{k+1}^{n+1}$ and $\mathcal{I}_{k+1}^{n+1}$
9:          Project $y^{k,n+1}$ according to $\mathcal{A}_{k+1}^{n+1}$ and update constraints
10:        **if** $\mathcal{A}_{k+1}^{n+1} = \mathcal{A}_k^{n+1}$ and the Newton update norm is reduced appropriately **then**
11:          Exit inner while loop
12:        **else if** Newton update norm is not reduced appropriately or maximal Newton iteration number is reached **then**
13:          Reduce time step size and go to Line 3
14:        **else**
15:          Update $k + 1 \rightarrow k$ and go to Line 7
16:        **end if**
17:      **end while**
18:      Advance time step via space and time algorithm [22, Algorithm 1]
19: **end while**

---

4. Numerical Studies

In this section we analyze our numerical results for the presented model of Section 2 with the adaptive finite element solver from Section 3. Firstly, we introduce and specify the simulation setup in Subsection 4.1. Secondly, we consider the numerical results in detail and discuss the physical effects as well as the numerical efficiency in Subsection 4.2. For this, we split the analysis in a 1D spherical symmetric case and a 2D quarter disk of a nanotube.

4.1. Simulation Setup

The derived model in Section 2 can be applied to cycle silicon as host material. The used model parameters as well as the normalized values are listed in Table 2. We apply an external lithium flux of $N_{\text{ext}} = 1$ C for lithiation and $N_{\text{ext}} = -1$ C for delithiation. During the simulations, the particles are cycled between $U_{\max} = 0.5$ V and $U_{\min} = 0.05$ V unless otherwise specified [31]. This corresponds to an initial concentration of around $c_0 = 0.02$ and a final time of close to 0.9, thus we set $t_{\text{end}} = 1.8$ for a total lithiation and delithiation cycle unless otherwise specified. At the beginning of the delithiation process, what is half of t_{end}, we continue with our adaptive algorithm, however, we change the sign of the external lithium flux and enforce for two time steps a time step size $\tau_n = 1 \times 10^{-6}$ as well as an order of one for the temporal adaptivity. The OCV curve for silicon is chosen as [65]:

$$U_{\text{OCV}}(z) = \frac{-0.2453z^3 - 0.00527z^2 + 0.2477z + 0.006457}{z + 0.002493}. \tag{42}$$

In the next parts we specify our geometrical reference domain for the representative battery particle including some further boundary conditions and symmetry assumption as well as some further implementation details.

4.1.1. Geometrical Setup

For a representative 3D spherical particle, the computational domain can be reduced to the 1D unit interval $\Omega_0 = (0, 1)$ with symmetry assumptions. The particle is surrounded by an obstacle like a core shell scenario, compare Figure 4. Then, the gap function g reduces to a one-dimensional parameter $g > 1$. The dimensional reduction introduces

Table 2: Model parameters for numerical experiments [31, 32].

Description	Symbol	Value	Unit	Dimensionless
Universal gas constant	R_{gas}	8.314	$\text{J mol}^{-1}\,\text{K}^{-1}$	1
Faraday constant	F	96485	$\text{J V}^{-1}\,\text{mol}^{-1}$	1
Operation temperature	T	298.15	K	1
Silicon				
Particle length scale	L_0	50×10^{-9}	m	1
Diffusion coefficient	D	1×10^{-17}	$\text{m}^2\,\text{s}^{-1}$	14.4
OCV curve	U_{OCV}	Equation (42)	V	$F/R_{\text{gas}}T \cdot (42)$
Young's modulus	E_{H}	90.13×10^9	Pa	116.74
Poisson's ratio	ν	0.22	–	0.22
Partial molar volume	ν_{pmv}	10.96×10^{-6}	$\text{m}^3\,\text{mol}^{-1}$	3.41
Maximal concentration	c_{max}	311.47×10^3	mol m^{-3}	1
Initial concentration	c_0	6.23×10^3	mol m^{-3}	2×10^{-2}

an artificial boundary Γ_0 at which we impose a no flux condition for the lithium flux and fixed radial displacement:

$$N \cdot n_0 = 0, \qquad u = 0 \qquad \text{on } (0, t_{\text{end}}) \times \Gamma_0. \tag{43}$$

At the particle surface Γ_{ext} the boundary conditions are considered as stated in Section 2. Assuming spherical symmetry we adapt the quadrature weight to $\mathrm{d}X_0 = 4\pi r^2\,\mathrm{d}r$ in the discrete finite element formulation. In this setting, we apply a constant initial concentration c_0, the chemical potential $\mu_0 = \partial_c \psi_{\text{ch}}(c_0)$ and the one-dimensional stress-free radial displacement $u_0(c_0) = r\,(\lambda_{\text{ch}}(c_0) - 1)$.

For the 2D simulation we rely on a silicon nanotube [25, 65] and reduce the domain to a quarter disk of the nanotube, see Figure 5. Here, we assume symmetry with respect to the x- and y-axis and no variations in z-direction. The nanotube is surrounded by a cuboid that will serve as a rigid obstacle. This results in two artificial boundaries $\Gamma_{0,x}$ and $\Gamma_{0,y}$ in axial direction and a curved boundary Γ_{ext} for the surface of the nanotube. On Γ_{ext} we apply an isoparametric mapping for the representation of the curved boundary. No flux conditions and only radial displacement is expected on the boundaries in axial direction:

$$N \cdot n_0 = 0, \qquad u_y = 0, \qquad \text{on } (0, t_{\text{end}}) \times \Gamma_{0,x}, \tag{44a}$$

$$N \cdot n_0 = 0, \qquad u_x = 0, \qquad \text{on } (0, t_{\text{end}}) \times \Gamma_{0,y}, \tag{44b}$$

where u_i is the i-th entry of the vector u, $i \in \{x, y\}$. For the starting values for the Newton method we choose a constant initial concentration c_0, $\mu_0 = 0$ and $u_0 = 0$.
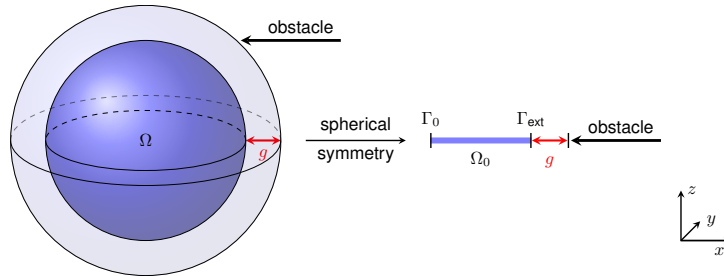

Figure 4: Dimension reduction of a three-dimensional unit sphere with surrounded obstacle to the one-dimensional unit interval with spherical symmetry and the gap function g, based on [23, Figure B.1].
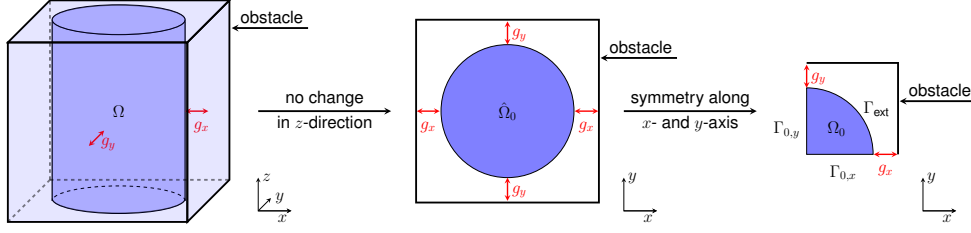
13

Figure 5: Dimension reduction of a three-dimensional nanowire with surrounded rectangular obstacle to the two-dimensional quarter disk and the (time-independent) quadratic obstacle with the gap function $(g_x, g_y)^\mathsf{T} = \boldsymbol{g} = \hat{\boldsymbol{g}} - \boldsymbol{X}_0 = (\hat{g}_x, \hat{g}_y)^\mathsf{T} - (X_{0,x}, X_{0,y})^\mathsf{T}$ with the components g_x and g_y in x- and y-directions, respectively.

4.1.2. Implementation Details

For our implementation, we apply an isoparametric fourth-order Lagrangian finite element method. The basis for our numerical simulation is the finite element library `deal.II` [50], implemented in `C++`, together with the interface to the Trilinos library [84, Version 12.8.1] and the UMFPACK package [85, Version 5.7.8] for the LU-decomposition. All simulations are executed on a desktop computer with 64 GB RAM, Intel i5-9500 CPU, GCC compiler version 10.3 and the operating system Ubuntu 20.04.5 LTS. The OpenMP Version 4.5 is used for shared memory parallelization for assembling the Newton matrix, residuals and spatial estimates.

Unless otherwise stated we choose for the space and time adaptive algorithm the tolerances $\mathrm{RelTol}_t = \mathrm{RelTol}_x = 1 \times 10^{-5}$ and $\mathrm{AbsTol}_t = \mathrm{AbsTol}_x = 1 \times 10^{-8}$. For the marking parameters for local coarsening and refinement, $\theta_c = 0.05$ and $\theta_r = 0.5$ are used and a maximal time step size $\tau_{\max} = 1 \times 10^{-2}$.

To get a diagonal structure for the mass matrix $\mathbf{B}_h$ or $\mathbf{D}_h$, respectively, we use mass lumping with a Gauß–Lobatto quadrature rule, compare Remark 1 in [48]. We initialize the active set $\mathcal{A}_k = \emptyset$ and the inactive set $\mathcal{I}_k = \mathcal{P}$ for the lithiation process. During lithiation we check in each time step the condition $\hat{u}_p - \hat{g}_p > 0$ to set this nodal point active, since $\hat{\lambda}_p = 0$ is zero due to the boundary condition for $p \in \mathcal{P}$. During delithiation we check in each time step $\hat{\lambda}_p \leq 0$ to set this nodal point inactive again, since $\hat{u}_p - \hat{g}_p = 0$. To increase numerical stability we only change to active points during lithiation and to inactive points during the following delithiation.

4.2. Numerical Results

This subsection discusses the numerical simulation results for our two presented computational domains: a 1D unit interval with modified quadrature weight to consider a 3D spherical particle and a 2D quarter nanotube. We analyze the behavior of concentration and stress development inside the representative active particle and show the efficiency of the adaptive space and time algorithm for cycling battery active particles with mechanical constraints.

4.2.1. 1D Spherical Symmetry

In this part we consider for one cycle the influence of the obstacle for the 1D spherical symmetric case as shown in Figure 4. Firstly, we compare the stress development of a configuration with and without obstacle. Secondly, have a closer look on the stress development regarding the radius of the particle as well as the concentration process. Thirdly, we investigate the influence of the size of the gap function on the stress development. We close the part with the consideration of the time step size comparing again a setup with and without obstacle.

In Figure 6 we see the absolute value of the maximal hydrostatic stress $|\sigma_\mathrm{h}| = |1/3\sigma_\mathrm{r} + 2/3\sigma_\phi|$ in GPa over the SOC, computed with the radial and tangential Cauchy stress, denoted with σ_r and σ_ϕ, respectively. The solid lines represent the lithiation process and the dashed lines the delithiation process in each case: once without and once with obstacle. For the gap function, we use $g = 0.4$. Before the particle gets in contact with the obstacle, the stress curves for the case without and with obstacle are identical. Shortly after the start of the lithiation process, a peak of around 0.8 GPa rises. This can be explained due to the characteristic behavior of the OCV curve, compare Figure 2 in [32]. At around SOC = 0.51, the particle gets in contact with the obstacle and the stress profiles deviate between the cases. After a short reduction, the stress values increase significantly until it reaches a maximum of $|\sigma_\mathrm{h,max}| \approx 5.36\,\mathrm{GPa}$. The short stress reduction results from the fact, that all (also positive) stress values inside the particle will change to compressive stresses which have negative values. So tensile stresses with a positive value have to go through the zero
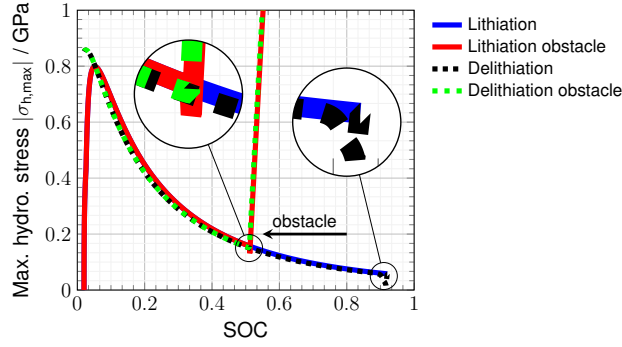
Figure 6: Comparison of the absolute value of the maximal hydrostatic stress $|\sigma_h|$ over the SOC for a cycle of a 1D spherical symmetric setup without and with obstacle.

point. Compare for this also the detailed analysis in Figure 7(b) to (c). The stress development in the case without obstacle flattens out until the change of the external lithium flux for SOC = 0.92 enters. Here again we have a short drop of the stress value due to the rearrangement from tensile to compressive values and vice versa. Because of the OCV curve, the stress values increase again but have a slight shift which can be explained by the rearrangement of the stress after the change from positive to negative lithium flux. After the particle detached from the obstacle again, the cases without and with obstacle coincide again ending at higher stress values.
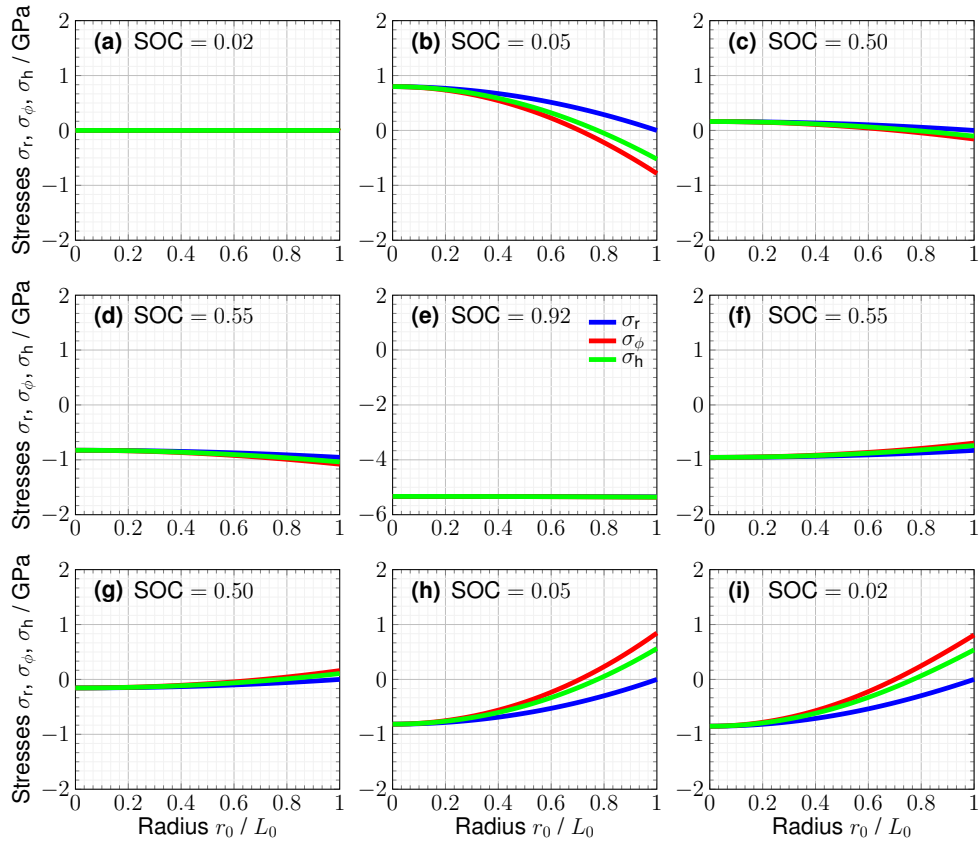

Figure 7: Stress development for the radial σ_r (blue), tangential σ_ϕ (red) and hydrostatic part σ_h (green) over the particle radius for nine different SOC $\in \{0.02, 0.05, 0.50, 0.55, 0.92, 0.55, 0.50, 0.05, 0.02\}$ for one cycle in (a)–(i), respectively.

15

In the next step we want to have a closer look on the stress distribution over the particle radius in the Lagrangian domain. In Figure 7 the three different stresses, radial, tangential and hydrostatic stress, are displayed over the particle radius for nine different SOC $\in \{0.02, 0.05, 0.50, 0.55, 0.92, 0.55, 0.50, 0.05, 0.02\}$ considering one cycling. At the initial SOC = 0.02 in Figure 7(a) there are no stresses present. At SOC = 0.05 the maximal values arise in the particle center at $r_0 = 0$. Here, tensile stresses occur whereas at the particle surface at $r_0 = 1$ the tangential stresses are compressive. Note the zero value for the radial stress σ_r. This is exactly the stress-free boundary condition in Equation (9) or Equation (12e) fulfilled with equality. In addition, tangential stresses are not equal to zero. For larger SOC all stresses decrease due to the influence of the OCV curve. A good qualitative accordance of our numerical results is given with the particle stresses in [31] neglecting the SEI results. At about SOC = 0.51 the particle touches the obstacle and the stress-free condition changes to a Dirichlet boundary condition for the displacement. The displacement is fixed now, we have Equation (12f) with equality. However, now negative stresses may occur to fulfill Equation (12e) with strict inequality. Exactly this can be seen in Figure 7(d) until the end of the lithiation at SOC = 0.92 in Figure 7(e). Here large comprehensive stresses appear throughout the particle domain. Note the different range on the stress axis in Figure 7(e). Changing now the sign of the external flux the discharging begins. In Figure 7(f) we are close to the point where the particle detached from the obstacle again. Compared to Figure 7(d) the curvature of the stress profiles is opposite. At SOC = 0.50 the particle has no contact to the obstacle any more and the stress-free boundary condition comes into effect again. At the end of the delithiation process the stress values are qualitatively similar to those of the lithiation process but have the opposite curvature resulting from the negative sign of the external lithium flux N_{ext}. In the end in Figure 7(i) the discharging process stops at a significant level of stress values compared to the constant initial concentration. Compared to the stress measurements in [86] investigating coated silicon electrodes, we have larger stress values. This could be due to the fact that our model is only based on a chemo-elastic approach. Nevertheless, our model is capable to deal with the change of the boundary condition during cycling.

In Figure 8 the concentration profile at the SOC $\in \{0.02, 0.20, 0.50, 0.92\}$ for the lithiation in blue and SOC $\in \{0.87, 0.55, 0.30, 0.05\}$ for the delithiation in green is shown over the particle radius r_0. We choose slightly different SOC values for the delithiation to have more distance between the different results. After the constant initial concentration c_0 the concentration profile increases with a slight curvature until its maximal value at SOC = 0.92. Note that the obstacle contact has no critical influence on the concentration profile. After switching to the delithiation process the curvature of the concentration is also opposite like for the stresses in Figure 7. The curvature remains also at the end of the simulation time for low concentration level.

Figure 9 shows the influence on the gap function on the stress development up to a maximal value of 6.0 GPa over the SOC. The above investigated case with $g = 0.4$ is here displayed with the blue dashed line. The simulation without an obstacle is shown with the solid black line. The smaller the gap function g is, the earlier the absolute value of the maximal hydrostatic stress rises. Likewise, the gradient of the stress profile increases with lower values of the gap function g. Interestingly, the rise of the stress development is not constant. For smaller gap function values is the slope significantly higher than for larger gap function values. Additionally, the gradient values decrease for higher
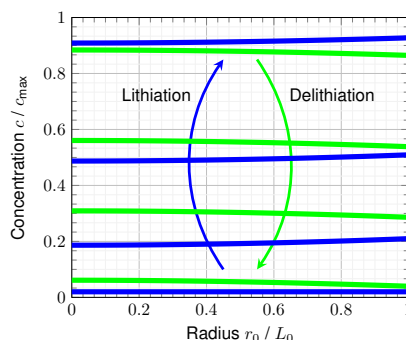

Figure 8: Concentration profile c over the particle radius r_0 during one charging (blue) and discharging (green) cycle at different SOC $\in \{0.02, 0.20, 0.50, 0.92, 0.87, 0.55, 0.30, 0.05\}$.
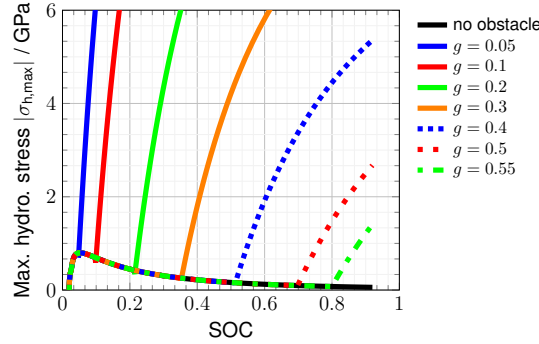
16

Figure 9: Study on different values for the gap function g: stress profiles for the absolute values of the maximal hydrostatic stress $|\sigma_{\mathrm{h,max}}|$ (colored) over the SOC compared to the case without obstacle in black for the charging process only.

SOC which could be explained by the lower curvature of the stress profile itself for larger stress values, see Figure 7(e) compared to, e.g., Figure 7(c), (d), (f) or (g).

In the last part of this section, we want to emphasize the need and the efficiency of the space and time adaptive algorithm. In Figure 10(a) the time step size τ_n and in Figure 10(b) the number of DOFs are plotted over the SOC without and with obstacle ($g = 0.4$) for the lithiation (solid) and the delithiation (dashed) process, respectively. We start the simulation with $\tau_0 = 1 \times 10^{-6}$ and 1539 DOFs in total. After a few time steps the gradients in concentration, chemical potential and displacement have formed and the time step size becomes larger until the maximal time step size of $\tau_{\mathrm{max}} = 0.01$. In the same time, the number of DOFs decreases since no new gradients occur. However, the time step size decreases significantly over three orders of magnitudes in the moment when the particle touches the obstacle, see Figure 10(a) at SOC = 0.51. After the particle is in contact with the obstacle, the time step size increases until τ_{max} again. When the delithiation process sets in, we see three crucial points: firstly, in Figure 10(a) the time step size of $\tau_n = 1 \times 10^{-6}$ for the delithiation with obstacle seems to be enough. Secondly, this is in contrast to the case without obstacle. Here, a drop of order of magnitude over more than six is needed compared to the maximal time step size τ_{max}. Thirdly, the number of DOFs behave in a similar way. More DOFs are needed in the case without obstacle compared to the case with obstacle. An explanation might be the again the lower curvature in the obstacle case so the changes in the gradients are not so large compared to the obstacle-free situation. After all gradients feature a reversed direction, the time step size τ_n increases as well as the number of DOFs decreases again. In the obstacle case the number of DOFs is even slightly lower compared to the simulation without obstacle. However, the time step size τ_n drops down to approximately the same level as for the charging process when the particle detaches from the obstacle. Finally, the time step size τ_n flattens out at the end of the simulation time. All in all, the efficiency of the spatial and temporal adaptive algorithm is clearly visible and of significant importance due to the switching point of the obstacle
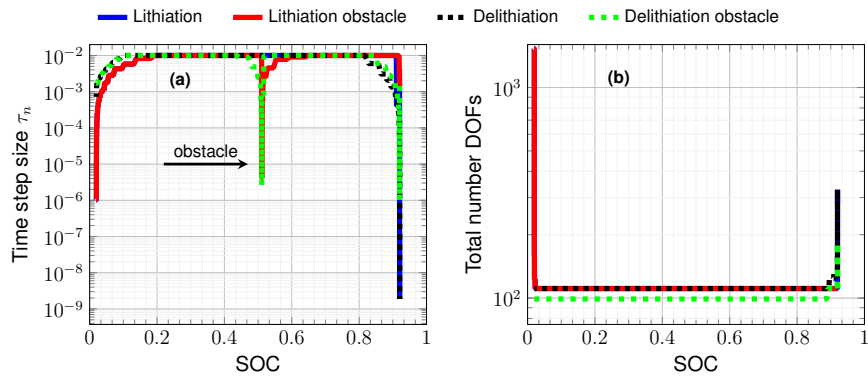

Figure 10: Time step size τ_n (a) and total number DOFs (b) over the SOC for charging and discharging without and with obstacle ($g = 0.4$).

17

contact and the switching point of the lithium flux. Without the adaptivity in space and time we would have to use the lowest time step size and the highest number of DOFs throughout the total simulation. See for more details about the numerical efficiency for phase-field materials [22, Section 4.3].

4.2.2. 2D Quarter Nanotube

Here we analyze the numerical results of the 2D quarter disk as described in Subsection 4.1. For this simulation we use the parameters $\theta_c = 0.005$, $\text{RelTol}_t = \text{RelTol}_x = 4 \times 10^{-5}$, $\text{AbsTol}_t = \text{AbsTol}_x = 4 \times 10^{-8}$. Furthermore, we choose $\tau_0 = 1 \times 10^{-8}$, $\tau_{\max} = 1 \times 10^{-3}$ and $t_{\text{end}} = 0.2$ to get an appropriate cycling and use a constant grid and a constant time step size for two time steps after the discharge process is started. To increase numerical stability during the time steps with active points, we accept this time step after one spatial refinement if the Newton update criterion is fulfilled and also in one following time step, we allow to skip the spatial refinement criterion. The time-independent $\hat{\boldsymbol{g}}$ is defined by $\hat{\boldsymbol{g}} = (\hat{g}_x, \hat{g}_y)^{\mathsf{T}} = (1.07, 1.07)^{\mathsf{T}}$.

In Figure 11(a)–(f) the von Mises stress in the general plane state

$$\sigma_{\text{vM}} = \sqrt{\sigma_{11}^2 + \sigma_{22}^2 - \sigma_{11}\sigma_{22} + 3\sigma_{12}^2} \tag{45}$$

is displayed for six different SOC $\in \{0.02, 0.07, 0.10, 0.12, 0.10, 0.02\}$ warped by the displacement vector to the Eulerian domain Ω and surrounded by the obstacle. The uniform grid for the initial time step without any stresses is shown in Figure 11(a). At SOC = 0.07 there are twelve active points, six at the lower right corner and six at the upper left corner. At this state all stresses are below 2.0 GPa but it is visible that the largest stresses occur at the contact points. This observation strengthens for higher SOC. The highest stress values occur at the first contact points, compare, e.g., Figure 11(c) or (d). This results from the suppression of the volume increase of the host material. Note that we charge and discharge with a constant lithium flux N_{ext}. At this point a Butler–Volmer boundary condition might be more appropriate but we postpone this to future work. Near new contact points we have a higher grid resolution due to changes mainly in the concentration profile. This point is discussed in more detail in Figure 12. Figure 11(d) is
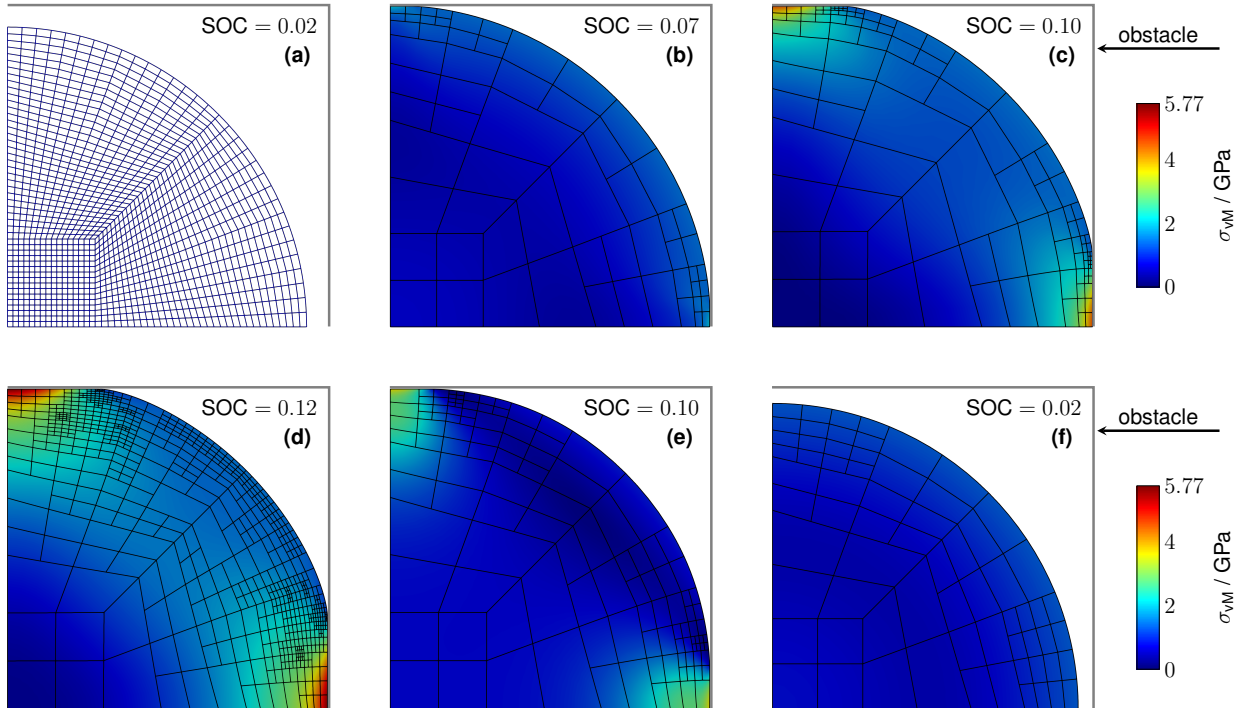

Figure 11: Von Mises stress σ_{vM} of the two-dimensional quarter disk of a nanotube in the Eulerian domain Ω surrounded by a square shaped obstacle at different SOC $\in \{0.02, 0.07, 0.10, 0.12, 0.10, 0.02\}$ for charging and discharging with $t_{\text{end}} = 0.2$.
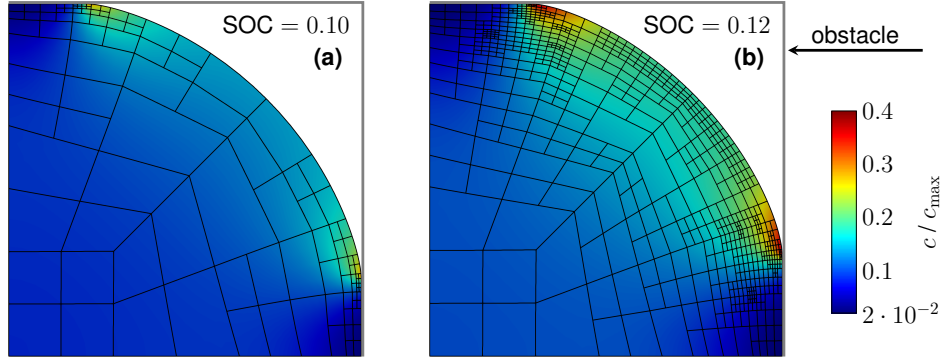
Figure 12: Concentration c of the two-dimensional quarter disk of a nanotube in the Eulerian domain Ω surrounded by a square shaped obstacle at SOC = $0.10, 0.12$.

at SOC = 0.119995, shortly after the discharging process was started. Here, the largest stress values occur which are again larger than the measured stresses in [86]. Similar to the 1D simulation a higher grid resolution and small time steps appear due to the change in the sign of the constant lithium flux N_{ext}. Again, the efficiency of the space and time adaptivity is crucial to appropriately capture the change in the physics. At SOC = 0.10 of the delithiation process in Figure 11(e) the grid has a coarser structure again. However, the stress distribution differs from SOC = 0.10 of the lithiation process. The occurring maximal stress values are lower and the distribution of the high values is more orientated towards the axes-direction instead of the obstacle direction. Moreover, the particle sections which are in contact with the obstacle are smaller, too. We also take notice of a dark blue region of low stresses that appears orthogonal to the first bisector of the coordinate system. In Figure 11(f) the final time $t_{end} = 0.2$ is reached with state of low stresses.

The concentration c for the two SOC-values 0.10 and 0.12 is shown in Figure 12. The result in Figure 12(a) emerged by the charging case, whereas Figure 12(b) arose at the same SOC = 0.119995 as in Figure 11(d). Eye-catching is the concentration profile near the obstacle contact. The region where the particle is in contact with the obstacle has a significantly lower concentration value compared with the region where the particle in not yet in touch with the obstacle. This effect is even more pronounced in Figure 12(b) than in Figure 12(a). Compared to the 1D spherical symmetry setup we have now a different behavior for the concentration around the obstacle. The region contacting the obstacle has lower concentration values possibly because the free energy density is smaller in the contact region with a chemical part with lower concentration values and a larger elastic part due to the obstacle contact. Also the gradient in the concentration profile as well as the one in the chemical potential has to be reverted leading to the finer grid distribution during the discharging process.
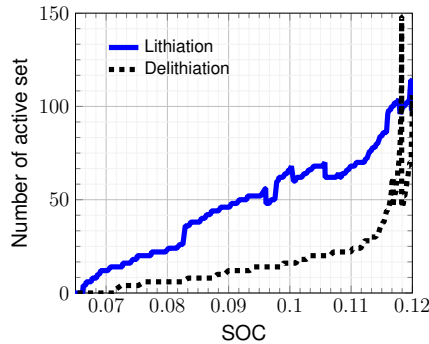

Figure 13: Number of active set $\mathcal{A}$ over the part of the SOC with a nonempty active set of the two-dimensional quarter disk of a nanotube surrounded by a square shaped obstacle for charging (solid blue) and discharging (dashed black) with $t_{end} = 0.2$.

19

Figure 13 presents the number of DOFs of the active set $\mathcal{A}$ over the SOC when the particle is in contact with the obstacle during cycling. A hysteresis in the number of DOFs is clearly visible. Specifically, the first active points arise at an earlier SOC whereas the last active points vanish at a larger SOC. The approximately linear increase of the number of active points is interrupted in the middle part by some sudden peaks and lows due to the refining and coarsening mechanism. In the end of charging the increase is again nearly linear except for two refinement peaks. During delithiation the number of active points has one large peak at SOC = 0.118252 resulting from the change of the gradient of the concentration and the chemical potential. This change is located a little further inside the particle and not directly at the boundary and therefore has a little delay in time. After the curvatures are rearranged the number of active points decrease with a smaller slope compared to the charging until the particle detaches from the obstacle. The total number of DOFs varies between a range of 3596 and 96164 DOFs and time step sizes τ_n between 1.58×10^{-8} and $\tau_{max} = 1 \times 10^{-3}$. The total computational time of this two dimensional setup is less than 37 minutes using the strength of the semismooth space and time adaptive algorithm.

5. Summary and Conclusion

We have developed a thermodynamically consistent chemo-mechanical model for battery active particles coupling chemical effects in the energy density dependent on a measured OCV curve and finite deformations together with mechanical boundary constraints of the obstacle problem during cycling of lithium-ion batteries. Furthermore, we have combined the primal-dual active set strategy as semismooth Newton method to the space and time adaptive solution algorithm with higher-order finite elements for the numerical simulation of our model equations. Using silicon as an example for a host material we have investigated several simulation setups in one and two dimensions to discuss the simulation results from a physical and numerical point of view. We have figured out that the stresses increase significantly if the particle has only limited surrounding space and is in contact with the obstacle. The distance to the obstacle has a crucial influence on the slope of the stress increase during cycling. Because of the switch in the sign of the external lithium flux the curvature of the concentration, chemical potential and stress profiles also have to rearrange oppositely resulting in a hysteresis development of the concentration, chemical potential and stress profiles. Although in the one-dimensional simulation setup the obstacle has almost no influence on the concentration over the particle radius, a clear difference can be seen in the two-dimensional case: a new lithium-poor region occurs near the obstacle area reducing the energy density due to the large ratio of the elastic part. In the two-dimensional case, the largest stress values occur near the first contact area between the active particle and the obstacle and a clear hysteresis of the stress values can be seen.

Looking at the time step scale the power of the adaptive method is revealed immediately. Without a variable time step size and order, the simulation must run with the smallest present time step size, e.g., using a standard backward Euler scheme to correctly capture all physical effects. This would result in a significant increase of computational costs compared to our numerical solution procedure. This is especially crucial for the change of the sign for the lithium flux to simulate a total cycling and also for long term battery operations. Similarly, the spatial adaptivity is necessary to appropriately capture all physical mechanisms, especially the new phenomena of the lithium-poor phase around the obstacle contact in the two-dimensional setup. The usage of the semismooth Newton method does not increase the number of DOFs of the linear system solving for the Newton update and makes it very useful for higher-dimensional computations [37].

The efficient extension to various two- and three-dimensional geometries with differently shaped particles and surrounded obstacles can be investigated in future works together with long term battery cycles. The large emerging stresses can lead to the need of further coupling, e.g., with plastic effects or additional fracture mechanisms. All this together can help in the understanding of mechanical degradation, capacity fade and battery aging. The investigation of numerically expensive simulations like for phase separation materials as LFP or LMO with surrounded obstacles is also another promising application for this highly efficient adaptive solver.

Declaration of competing interest

The authors declare that they have no known competing financial interests or personal relationships that could have appeared to influence the work in this paper.

CRediT authorship contribution statement

R. Schoof: Methodology, Software, Validation, Formal analysis, Investigation, Data Curation, Writing – original draft, Visualization. **G. F. Castelli:** Software, Data Curation, Writing – review & editing. **W. Dörfler:** Conceptualization, Resources, Writing – review & editing, Supervision, Project administration, Funding acquisition.

Acknowledgement

ORCID

R. Schoof: https://orcid.org/0000-0001-6848-3844
G. F. Castelli: https://orcid.org/0000-0001-5484-6093
W. Dörfler: https://orcid.org/0000-0003-1558-9236

Appendices

A. Abbreviations and Symbols

Abbreviations

DAE	differential algebraic equation	NCP	nonlinear complementary problem
DOF	degree of freedom	OCV	open circuit voltage
KKT	Karush–Kuhn–Tucker	SOC	state of charge

Symbol	Description		
Latin symbols		Greek symbols	
$_z\mathbf{A}_h(z, \mathbf{G})$	partial derivative of $\mathbf{A}_h$ regarding z	$\alpha > 0$	coefficient in NCP function
$_{\mathbf{G}}\mathbf{A}_h(z, \mathbf{G})$	partial derivative of $\mathbf{A}_h$ regarding $\mathbf{G}$	$\alpha_{\tau_n} > 0$	coefficient for adaptive time discretization
$\mathscr{A}$	set of all active nodes of $\mathcal{P}$		
$\mathbf{B}_h$	discrete auxiliary matrix	$\delta_{j,k}$	Kronecker delta
C	NCP function	$\Gamma_{\mathcal{P}}$	potential contact zone
$\mathbb{C}$	fourth-order stiffness tensor	λ	Lagrange multiplier
$\mathbf{D}_h$	discrete diagonal matrix	λ_{ch}	factor of concentration induced deformation gradient
$\mathbf{E}_{\mathrm{el}}$	elastic strain tensor		
$\mathbf{F} = \boldsymbol{\nabla}_0 \chi$	deformation gradient tensor	μ	chemical potential
$\mathbf{F} = \mathbf{F}_{\mathrm{ch}}\mathbf{F}_{\mathrm{el}}$	multiplicative decomposition of $\mathbf{F}$	ν	Poisson's ratio
$\mathbf{F}_{\mathrm{ch}}$	chemical deformation gradient	Ω	Eulerian domain
$\mathbf{F}_{\mathrm{el}}$	elastic deformation gradient	Ω_0	Lagrangian domain
g	gap function	φ	scalar valued test function
$\hat{g}$	projection	ψ	total free energy density
$\mathcal{I}$	set of all inactive nodes of $\mathcal{P}$	ψ_{ch}	chemical part of free energy density

m	scalar valued mobility	ψ_{el}	elastic part of free energy density
$\boldsymbol{n}, \boldsymbol{n}_0$	normal vector on Ω, Ω_0	$\boldsymbol{\sigma}$	Cauchy stress tensor
N, N_Λ	number of nodes of V_h, Λ_h	$\boldsymbol{\xi}_j$	vector valued test function of node j
$\boldsymbol{N}$	lithium flux	ξ_j	scalar basis function: nonzero entry
N_{ext}	external lithium flux		of $\boldsymbol{\xi}_j$ of node j
$\mathcal{N}$	set of all other nodes of Ω_0: $\mathcal{S}\backslash\mathcal{P}$	**Mathematical symbols**	
$\mathbf{P}$	first Piola–Kirchhoff stress tensor	$\partial\Omega_0$	boundary of Ω_0
$\mathcal{P}$	set of all potential contact nodes on $\Gamma_{\mathcal{P}}$	$\boldsymbol{\nabla}_0$	gradient vector in Lagrangian domain
$\mathcal{S}$	set of all nodes on Ω_0	$\square:\tilde{\square}$	reduction of two dimensions of
U_{OCV}	OCV curve		two tensors $\square$ and $\tilde{\square}$
$\boldsymbol{u} = \boldsymbol{x} - \boldsymbol{X}_0$	displacement vector	**Indices**	
$\boldsymbol{u}_h$	discrete displacement vector or	$\square_0$	considering variable in Lagrangian
	algebraic representation		domain or initial time
V	scalar valued function space	$\square_h$	finite dimensional function of $\square$ or
$\boldsymbol{V}$	vector valued function space		algebraic representation of $\square$ with
V^*	subset of V		respect to basis function
V^+	subset of V^*	$\square_{\mathcal{P}}$	discrete vector with all entries on set $\mathcal{P}$
$\boldsymbol{x} = \boldsymbol{\chi}(t, \boldsymbol{X_0})$	motion	$\partial_{\square}$	partial derivative with respect to $\square$
$\boldsymbol{X}_0$	space coordinate in Lagrangian domain		

B. Tensor Analysis

We use the following notation for a scalar $a \in \mathbb{R}$, first-order vectors $\boldsymbol{b}, \boldsymbol{c} \in \mathbb{R}^d$, second-order tensors $\mathbf{A}, \mathbf{B}, \mathbf{C} \in \mathbb{R}^{d,d}$, the second-order identity $\mathbf{Id} \in \mathbb{R}^{d,d}$ and a fourth-order tensor $\mathbb{C} \in \mathbb{R}^{d,d,d,d}$:

$$a = \boldsymbol{b} \cdot \boldsymbol{c}, \qquad \mathbf{A} = \mathbf{BC}, \qquad \mathbf{A} = \mathbb{C}\left[\mathbf{B}\right], \qquad a = \mathbf{A}:\mathbb{C}\left[\mathbf{B}\right] \tag{B.1}$$

$$a = \mathbf{B}:\mathbf{C} = \mathrm{tr}\left(\mathbf{B}^{\mathsf{T}}\mathbf{C}\right) = \mathrm{tr}\left(\mathbf{C}^{\mathsf{T}}\mathbf{B}\right) = \mathrm{tr}\left(\mathbf{BC}^{\mathsf{T}}\right) = \mathrm{tr}\left(\mathbf{C}^{\mathsf{T}}\mathbf{B}\right) = \mathbf{C}:\mathbf{B}, \tag{B.2}$$

where $\mathrm{tr}\left(\mathbf{A}\right)$ denotes the trace of a tensor $\mathbf{A}$. Further, we write for first-order vectors $\boldsymbol{a}$, $\boldsymbol{b}$ and $\boldsymbol{c} \in \mathbb{R}^d$:

$$\boldsymbol{a} = \left[\boldsymbol{b}\right]\left[\boldsymbol{c}\right] \tag{B.3}$$

as $a_i = b_i c_i$ for all $i = 1, \ldots d$ and for a vector $\boldsymbol{a} \in \mathbb{R}^d$, we write for a set $\mathcal{P}$ with $|\mathcal{P}| < d$:

$$\boldsymbol{a}_{\mathcal{P}} = \boldsymbol{0} \tag{B.4}$$

as $a_p = 0$ for all $p = 1, \ldots, |\mathcal{P}|$, understood componentwise respectively.

Moreover, we write for the scalar product for two scalar valued functions $f, g \in L^2(\Omega_0)$

$$(f, g) = \int_{\Omega_0} f g \,\mathrm{d}\boldsymbol{X}_0, \tag{B.5}$$

for the scalar product for two vector valued functions $\boldsymbol{f}, \boldsymbol{g} \in L^2(\Omega_0; \mathbb{R}^d)$

$$(\boldsymbol{f}, \boldsymbol{g}) = \int_{\Omega_0} \boldsymbol{f} \cdot \boldsymbol{g} \,\mathrm{d}\boldsymbol{X}_0 \tag{B.6}$$

and for the scalar product for two tensor valued functions $\mathbf{F}, \mathbf{G} \in L^2(\Omega_0; \mathbb{R}^{d,d})$

$$(\mathbf{F}, \mathbf{G}) = \int_{\Omega_0} \mathbf{F}:\mathbf{G} \,\mathrm{d}\boldsymbol{X}_0. \tag{B.7}$$

Boundary integrals for $\Gamma \subseteq \partial\Omega_0$ are denoted with the subscript of the respective boundary, e.g.,

$$(f, g)_{\Gamma} = \int_{\Gamma} f g \,\mathrm{d}\boldsymbol{S}_0. \tag{B.8}$$

22

References

[1] A. Tomaszewska, Z. Chu, X. Feng, S. O'Kane, X. Liu, J. Chen, C. Ji, E. Endler, R. Li, L. Liu, Y. Li, S. Zheng, S. Vetterlein, M. Gao, J. Du, M. Parkes, M. Ouyang, M. Marinescu, G. Offer, B. Wu, Lithium-ion battery fast charging: A review, eTransportation 1 (2019) 100011. doi:10.1016/j.etran.2019.100011.

[2] H. Tian, F. Xin, X. Wang, W. He, W. Han, High capacity group-IV elements (Si, Ge, Sn) based anodes for lithium-ion batteries, J. Materiomics 1 (3) (2015) 153–169. doi:10.1016/j.jmat.2015.06.002.

[3] P. Li, H. Kim, S.-T. Myung, Y.-K. Sun, Diverting exploration of silicon anode into practical way: A review focused on silicon-graphite composite for lithium ion batteries, Energy Stor. Mater. 35 (2021) 550–576. doi:10.1016/j.ensm.2020.11.028.

[4] R. Mo, X. Tan, F. Li, R. Tao, J. Xu, D. Kong, Z. Wang, B. Xu, X. Wang, C. Wang, J. Li, Y. Peng, Y. Lu, Tin-graphene tubes as anodes for lithium-ion batteries with high volumetric and gravimetric energy densities, Nat. Commun. 11 (1) (2020) 1374. doi:10.1038/s41467-020-14859-z.

[5] W.-J. Zhang, A review of the electrochemical performance of alloy anodes for lithium-ion batteries, J. Power Sources 196 (1) (2011) 13–24. doi:10.1016/j.jpowsour.2010.07.020.

[6] R. Xu, K. Zhao, Electrochemomechanics of electrodes in Li-ion batteries: A review, J. Electrochem. En. Conv. Stor. 13 (3) (2016) 030803. doi:10.1115/1.4035310.

[7] Y. Zhao, P. Stein, Y. Bai, M. Al-Siraj, Y. Yang, B.-X. Xu, A review on modeling of electro-chemo-mechanics in lithium-ion batteries, J. Power Sources 413 (2019) 259–283. doi:10.1016/j.jpowsour.2018.12.011.

[8] Y. C. Song, Z. Z. Li, A. K. Soh, J. Q. Zhang, Diffusion of lithium ions and diffusion-induced stresses in a phase separating electrode under galvanostatic and potentiostatic operations: Phase field simulations, Mech. Mater. 91 (2015) 363–371. doi:10.1016/j.mechmat.2015.04.015.

[9] C. Delmas, M. Maccario, L. Croguennec, F. Le Cras, F. Weill, Lithium deintercalation in LiFePO$_4$ nanoparticles via a domino-cascade model, Nat. Mater. 7 (8) (2008) 665–671. doi:10.1038/nmat2230.

[10] A. Van Der Ven, C. Marianetti, D. Morgan, G. Ceder, Phase transformations and volume changes in spinel Li$_x$Mn$_2$O$_4$, Solid State Ion. 135 (1–4) (2000) 21–32. doi:10.1016/S0167-2738(00)00326-X.

[11] A.-C. Walk, M. Huttin, M. Kamlah, Comparison of a phase-field model for intercalation induced stresses in electrode particles of lithium ion batteries for small and finite deformation theory, Eur. J. Mech. A Solids 48 (2014) 74–82. doi:10.1016/j.euromechsol.2014.02.020.

[12] J. W. Cahn, J. E. Hilliard, Free energy of a nonuniform system. I. Interfacial free energy, J. Chem. Phys. 28 (2) (1958) 258–267. doi:10.1063/1.1744102.

[13] J. W. Cahn, Free energy of a nonuniform system. II. Thermodynamic basis, J. Chem. Phys. 30 (5) (1959) 1121–1135. doi:10.1063/1.1730145.

[14] F. Larché, J. W. Cahn, A linear theory of thermochemical equilibrium of solids under stress, Acta Metallurgica 21 (8) (1973) 1051–1063. doi:10.1016/0001-6160(73)90021-7.

[15] H. Garcke, M. Rumpf, U. Weikard, The Cahn–Hilliard equation with elasticity—finite element approximation and qualitative studies, Interfaces Free Bound. 3 (1) (2001) 101–118. doi:10.4171/IFB/34.

[16] H. Garcke, U. Weikard, Numerical approximation of the Cahn–Larché equation, Numer. Math. 100 (4) (2005) 639–662. doi:10.1007/s00211-004-0578-x.

[17] C. V. Di Leo, E. Rejovitzky, L. Anand, A Cahn–Hilliard-type phase-field theory for species diffusion coupled with large elastic deformations: Application to phase-separating Li-ion electrode materials, J. Mech. Phys. Solids 70 (2014) 1–29. doi:10.1016/j.jmps.2014.05.001.

[18] M. G. Hennessy, A. Münch, B. Wagner, Phase separation in swelling and deswelling hydrogels with a free boundary, Phys. Rev. E 101 (3) (2020) 032501. doi:10.1103/physreve.101.032501.

[19] M. Werner, A. Pandolfi, K. Weinberg, A multi-field model for charging and discharging of lithium-ion battery electrodes, Contin. Mech. Thermodyn. 33 (3) (2021) 661–685. doi:10.1007/s00161-020-00943-8.

[20] M. Huttin, M. Kamlah, Phase-field modeling of stress generation in electrode particles of lithium ion batteries, Appl. Phys. Lett. 101 (13) (2012) 133902–1–133902–4. doi:10.1063/1.4754705.

[21] T. Zhang, M. Kamlah, A nonlocal species concentration theory for diffusion and phase changes in electrode particles of lithium ion batteries, Contin. Mech. Thermodyn. 30 (3) (2018) 553–572. doi:10.1007/s00161-018-0624-z.

[22] G. F. Castelli, L. von Kolzenberg, B. Horstmann, A. Latz, W. Dörfler, Efficient simulation of chemical-mechanical coupling in battery active particles, Energy Technol. 9 (6) (2021) 2000835. doi:10.1002/ente.202000835.

[23] G. F. Castelli, Numerical investigation of Cahn–Hilliard-type phase-field models for battery active particles, Ph.D. thesis, Karlsruhe Institute of Technology (KIT) (2021). doi:10.5445/IR/1000141249.

[24] T. Zhang, M. Kamlah, Mechanically coupled phase-field modeling of microstructure evolution in sodium ion batteries particles of Na$_x$FePO$_4$, J. Electrochem. Soc. 167 (2) (2020) 020508. doi:10.1149/1945-7111/ab645a.

[25] L. Wu, V. De Andrade, X. Xiao, J. Zhang, Phase field modeling of coupled phase separation and diffusion-induced stress in lithium iron phosphate particles reconstructed from synchrotron nano x-ray tomography, J. Electrochem. En. Conv. Stor. 16 (4) (2019) 041006. doi:10.1115/1.4043155.

[26] T. Zhang, M. Kamlah, Sodium ion batteries particles: Phase-field modeling with coupling of Cahn–Hilliard equation and finite deformation elasticity, J. Electrochem. Soc. 165 (10) (2018) A1997–A2007. doi:10.1149/2.0141810jes.

[27] T. Zhang, M. Kamlah, Phase-field modeling of the particle size and average concentration dependent miscibility gap in nanoparticles of Li$_x$Mn$_2$O$_4$, Li$_x$FePO$_4$, and Na$_x$FePO$_4$ during insertion, Electrochim. Acta 298 (2019) 31–42. doi:10.1016/j.electacta.2018.12.007.

[28] L. Chen, F. Fan, L. Hong, J. Chen, Y. Z. Ji, S. L. Zhang, T. Zhu, L. Q. Chen, A phase-field model coupled with large elasto-plastic deformation: Application to lithiated silicon electrodes, J. Electrochem. Soc. 161 (11) (2014) F3164–F3172. doi:10.1149/2.0171411jes.

[29] K. Zhang, Y. Li, F. Wang, B. Zheng, F. Yang, A phase-field study of the effect of local deformation velocity on lithiation-induced stress in wire-like structures, J. Phys. D: Appl. Phys. 52 (2019) 145501. doi:10.1088/1361-6463/ab00dc.

[30] M. Poluektov, A. B. Freidin, L. Figiel, Modelling stress-affected chemical reactions in non-linear viscoelastic solids with application to lithiation reaction in spherical Si particles, Internat. J. Engrg. Sci. 128 (2018) 44–62. doi:10.1016/j.ijengsci.2018.03.007.

[31] L. von Kolzenberg, A. Latz, B. Horstmann, Chemo-mechanical model of sei growth on silicon electrode particles, Batter. Supercaps 5 (2) (2022) e202100216. doi:10.1002/batt.202100216.

[32] R. Schoof, G. F. Castelli, W. Dörfler, Parallelization of a finite element solver for chemo-mechanical coupled anode and cathode particles in lithium-ion batteries, in: T. Kvamsdal, K. M. Mathisen, K.-A. Lie, M. G. Larson (Eds.), 8th European Congress on Computational Methods in Applied Sciences and Engineering (ECCOMAS Congress 2022), CIMNE, 2022. doi:10.23967/eccomas.2022.106.

[33] T. A. Laursen, Computational contact and impact mechanics, Springer-Verlag, Berlin, Berlin, 2002.

[34] P. Wriggers, Computational contact mechanics, 2nd Edition, Springer, Berlin, 2006.

[35] K. Willner, Kontinuums- und Kontaktmechanik: synthetische und analytische Darstellung, Engineering online library, Springer, Berlin, 2003.

[36] P. Alart, A. Curnier, A mixed formulation for frictional contact problems prone to Newton like solution methods, Comput. Methods Appl. Mech. Engrg. 92 (3) (1991) 353–375. doi:10.1016/0045-7825(91)90022-X.

[37] S. Brunssen, F. Schmid, M. Schäfer, B. Wohlmuth, A fast and robust iterative solver for nonlinear contact problems using a primal-dual active set strategy and algebraic multigrid, Internat. J. Numer. Methods Engrg. 69 (3) (2007) 524–543. doi:10.1002/nme.1779.

[38] K. A. Fischer, P. Wriggers, Frictionless 2d contact formulations for finite deformations based on the mortar method, Comput. Mech. 36 (3) (2005) 226–244. doi:10.1007/s00466-005-0660-y.

[39] M. Hintermüller, K. Ito, K. Kunisch, The primal-dual active set strategy as a semismooth Newton method, SIAM J. Optim. 13 (3) (2002) 865–888 (2003). doi:10.1137/S1052623401383558.

[40] M. A. Puso, T. A. Laursen, A mortar segment-to-segment contact method for large deformation solid mechanics, Comput. Methods Appl. Mech. Engrg. 193 (6-8) (2004) 601–629. doi:10.1016/j.cma.2003.10.010.
URL https://doi.org/10.1016/j.cma.2003.10.010

[41] B. I. Wohlmuth, R. H. Krause, Monotone multigrid methods on nonmatching grids for nonlinear multibody contact problems, SIAM J. Sci. Comput. 25 (1) (2003) 324–347. doi:10.1137/S1064827502405318.

[42] A. Signorini, Sopra alcune questioni di elastostatica, Annali della Scuola Normale Superiore di Pisa - Scienze Fisiche e Matematiche 21 (2) (1933) 143–148.

[43] A. Signorini, Sopra alcune questioni di statica dei sistemi continui, Annali della Scuola Normale Superiore di Pisa - Scienze Fisiche e Matematiche 2 (2) (1933) 231–251.

[44] S. Hüeber, B. I. Wohlmuth, A primal-dual active set strategy for non-linear multibody contact problems, Comput. Methods Appl. Mech. Engrg. 194 (27-29) (2005) 3147–3166. doi:10.1016/j.cma.2004.08.006.

[45] S. Hüeber, M. Mair, B. I. Wohlmuth, A priori error estimates and an inexact primal-dual active set strategy for linear and quadratic finite elements applied to multibody contact problems, Appl. Numer. Math. 54 (3-4) (2005) 555–576. doi:10.1016/j.apnum.2004.09.019.

[46] S. Hüeber, A. Matei, B. Wohlmuth, A contact problem for electro-elastic materials, ZAMM Z. Angew. Math. Mech. 93 (10-11) (2013) 789–800. doi:10.1002/zamm.201200235.

[47] M. Hintermüller, V. A. Kovtunenko, K. Kunisch, Semismooth newton methods for a class of unilaterally constrained variational problems, Technical Report 270 Universität Graz/Technische Universität Graz. SFB F003-Optimierung und Kontrolle (2003).

[48] J. Frohne, T. Heister, W. Bangerth, Efficient numerical methods for the large-scale, parallel solution of elastoplastic contact problems, Internat. J. Numer. Methods Engrg. 105 (6) (2016) 416–439. doi:10.1002/nme.4977.

[49] C. Hager, B. I. Wohlmuth, Semismooth Newton methods for variational problems with inequality constraints, GAMM-Mitt. 33 (1) (2010) 8–24. doi:10.1002/gamm.201010002.

[50] D. Arndt, W. Bangerth, B. Blais, M. Fehling, R. Gassmöller, T. Heister, L. Heltai, U. Köcher, M. Kronbichler, M. Maier, P. Munch, J.-P. Pelteret, S. Proell, K. Simon, B. Turcksin, D. Wells, J. Zhang, The deal.II library, version 9.3, J. Numer. Math. 29 (3) (2021) 171–186. doi:10.1515/jnma-2021-0081.

[51] R. Kornhuber, R. Krause, Adaptive multigrid methods for Signorini's problem in linear elasticity, Comput. Vis. Sci. 4 (1) (2001) 9–20. doi:10.1007/s007910100052.

[52] O. Sander, C. Klapproth, J. Youett, R. Kornhuber, P. Deuflhard, Towards an efficient numerical simulation of complex 3D knee joint motion, Comput. Vis. Sci. 16 (3) (2013) 119–138. doi:10.1007/s00791-014-0227-6.

[53] J. C. De Los Reyes, S. González Andrade, A combined BDF-semismooth Newton approach for time-dependent Bingham flow, Numer. Methods Partial Differ. Equ. 28 (3) (2012) 834–860. doi:10.1002/num.20658.

[54] A. Lauser, C. Hager, R. Helmig, B. Wohlmuth, A new approach for phase transitions in miscible multi-phase flow in porous media, Adv. Water Resour. 34 (8) (2011) 957–966. doi:10.1016/j.advwatres.2011.04.021.

[55] P. Sa Ngiamsunthorn, A. Suechoei, P. Kumam, Optimal control for obstacle problems involving time-dependent variational inequalities with Liouville-Caputo fractional derivative, Adv. Differ. Equ. 2021 (2021) 298. doi:10.1186/s13662-021-03453-2.

[56] C. V. Di Leo, E. Rejovitzky, L. Anand, Diffusion-deformation theory for amorphous silicon anodes: The role of plastic deformation on electrochemical performance, Int. J. Solids Struct. 67-68 (2015) 283–296. doi:10.1016/j.ijsolstr.2015.04.028.

[57] G. F. Castelli, W. Dörfler, Study on an adaptive finite element solver for the Cahn–Hilliard equation, in: F. J. Vermolen, C. Vuik (Eds.), Numerical Mathematics and Advanced Applications ENUMATH 2019, Vol. 139 of Lecture Notes in Computational Science and Engineering, Springer, Cham, 2021, pp. 245–253. doi:10.1007/978-3-030-55874-1_23.

[58] G. A. Holzapfel, Nonlinear Solid Mechanics, John Wiley & Sons, Ltd., Chichester, 2000.

[59] D. Braess, Finite Elements, 3rd Edition, Cambridge University Press, Cambridge, 2007. doi:10.1007/978-3-540-72450-6.

[60] A. Latz, J. Zausch, Multiscale modeling of lithium ion batteries: thermal aspects, Beilstein J. Nanotechnol. 6 (2015) 987–1007. doi:10.3762/bjnano.6.102.

[61] A. Latz, J. Zausch, Thermodynamic consistent transport theory of Li-ion batteries, J. Power Sources 196 (6) (2011) 3296–3302. doi:10.1016/j.jpowsour.2010.11.088.

[62] M. Schammer, B. Horstmann, A. Latz, Theory of transport in highly concentrated electrolytes, J. Electrochem. Soc. 168 (2) (2021) 026511. doi:10.1149/1945-7111/abdddf.

[63] L. Anand, A Cahn–Hilliard-type theory for species diffusion coupled with large elastic-plastic deformations, J. Mech. Phys. Solids 60 (12) (2012) 1983–2002. `doi:10.1016/j.jmps.2012.08.001`.

[64] K. Zhang, Y. Li, J. Wu, B. Zheng, F. Yang, Lithiation-induced buckling of wire-based electrodes in lithium-ion batteries: A phase-field model coupled with large deformation, Int. J. Solids Struct. 144-145 (2018) 289–300. `doi:10.1016/j.ijsolstr.2018.05.014`.

[65] C. K. Chan, H. Peng, G. Liu, K. McIlwrath, X. F. Zhang, R. A. Huggins, Y. Cui, High-performance lithium battery anodes using silicon nanowires, Nat. Nanotechnol. 3 (1) (2007) 31–35. `doi:10.1038/nnano.2007.411`.

[66] P. Keil, S. F. Schuster, J. Wilhelm, J. Travi, A. Hauser, R. C. Karl, A. Jossen, Calendar aging of lithium-ion batteries, J. Electrochem. Soc. 163 (9) (2016) A1872–A1880. `doi:10.1149/2.0411609jes`.

[67] A. Latz, J. Zausch, Thermodynamic derivation of a Butler–Volmer model for intercalation in Li-ion batteries, Electrochim. Acta 110 (2013) 358–362. `doi:10.1016/j.electacta.2013.06.043`.

[68] V. Hoffmann, G. Pulletikurthi, T. Carstens, A. Lahiri, A. Borodin, M. Schammer, B. Horstmann, A. Latz, F. Endres, Influence of a silver salt on the nanostructure of a Au(111)/ionic liquid interface: An atomic force microscopy study and theoretical concepts, Phys. Chem. Chem. Phys. 20 (7) (2018) 4760–4771. `doi:10.1039/C7CP08243F`.

[69] A. Friedman, Variational principles and free-boundary problems, Pure and applied mathematics, Wiley, New York, 1982.

[70] R. Kornhuber, Adaptive Monotone Multigrid Methods for Nonlinear Variational Problems, 1st Edition, Advances in Numerical Mathematics, B. G. Teubner, Stuttgart, 1997.

[71] J. Haslinger, I. Hlaváček, Contact between elastic bodies. I. Continuous problems, Appl. Math. 25 (5) (1980) 324–347. `doi:10.21136/am.1980.103868`.

[72] P. Boieri, F. Gastaldi, D. Kinderlehrer, Existence, uniqueness, and regularity results for the two-body contact problem, Appl. Math. Optim. 15 (3) (1987) 251–277. `doi:10.1007/BF01442654`.

[73] I. Hlaváček, J. Haslinger, J. Nečas, J. Lovíšek, Solution of variational inequalities in mechanics, Vol. 66 of Applied Mathematical Sciences, Springer-Verlag, New York, 1988. `doi:10.1007/978-1-4612-1048-1`.

[74] D. Kinderlehrer, G. Stampacchia, An introduction to variational inequalities and their applications, Vol. 31 of Classics in Applied Mathematics, Society for Industrial and Applied Mathematics (SIAM), Philadelphia, PA, 2000. `doi:10.1137/1.9780898719451`.

[75] F. Ben Belgacem, P. Hild, P. Laborde, Extension of the mortar finite element method to a variational inequality modeling unilateral contact, Math. Models Methods Appl. Sci. 9 (2) (1999) 287–303. `doi:10.1142/S0218202599000154`.

[76] P. Hild, Numerical implementation of two nonconforming finite element methods for unilateral contact, Comput. Methods Appl. Mech. Engrg. 184 (1) (2000) 99–123. `doi:10.1016/S0045-7825(99)00096-1`.

[77] B. I. Wohlmuth, A mortar finite element method using dual spaces for the Lagrange multiplier, SIAM J. Numer. Anal. 38 (3) (2000) 989–1012. `doi:10.1137/S0036142999350929`.

[78] M. W. Reichelt, L. F. Shampine, J. Kierzenka, Matlab `ode15s`, copyright 1984–2020 The MathWorks, Inc. (1997).
URL `http://www.mathworks.com`

[79] L. F. Shampine, M. W. Reichelt, The MATLAB ODE suite, SIAM J. Sci. Comput. 18 (1) (1997) 1–22. `doi:10.1137/S1064827594276424`.

[80] L. F. Shampine, M. W. Reichelt, J. A. Kierzenka, Solving index-1 DAEs in MATLAB and Simulink, SIAM Rev. 41 (3) (1999) 538–552. `doi:10.1137/S003614459933425X`.

[81] L. F. Shampine, I. Gladwell, S. Thompson, Solving ODEs with MATLAB, Cambridge University Press, Cambridge, 2003. `doi:10.1017/CBO9780511615542`.

[82] M. Ainsworth, J. T. Oden, A Posteriori Error Estimation in Finite Element Analysis, Pure and Applied Mathematics, John Wiley & Sons, Inc., New York, 2000.

[83] L. Baňas, R. Nürnberg, Adaptive finite element methods for Cahn–Hilliard equations, J. Comput. Appl. Math. 218 (1) (2008) 2–11. `doi:10.1016/j.cam.2007.04.030`.

[84] T. Trilinos Project Team, The Trilinos Project Website (2020).
URL `https://trilinos.github.io`

[85] T. A. Davis, Algorithm 832: UMFPACK V4.3—an unsymmetric-pattern multifrontal method, ACM Trans. Math. Software 30 (2) (2004) 196–199. `doi:10.1145/992200.992206`.

[86] A. Al-Obeidi, D. Kramer, S. T. Boles, R. Mönig, C. V. Thompson, Mechanical measurements on lithium phosphorous oxynitride coated silicon thin film electrodes for lithium-ion batteries during lithiation and delithiation, Appl. Phys. Lett. 109 (7) (2016) 071902. `doi:10.1063/1.4961234`.